Advanced Guar Gum/Polyvinyl Alcohol/MnP-Based Smart Hydrogel for Promoting Osteoblastic Proliferation

Karen Guillén-Carvajal [†], Benjamín Valdez-Salas [*,†], Jorge Salvador-Carlos [*], Jimena Chairez-González, Ernesto Beltrán-Partida, Mario Curiel-Alvarez

Posted Date: 26 February 2026

doi: 10.20944/preprints202602.1380.v1

Keywords: stimuli-responsive biomaterial; multi-network; bone tissue engineering; osteoblast migration; skin biomaterials

 doi:10.20944/preprints202602.1380.v1

Article

Advanced Guar Gum/Polyvinyl Alcohol/MnP-Based Smart Hydrogel for Promoting Osteoblastic Proliferation

Karen Guillén-Carvajal †, Benjamin Valdez-Salas *,†, Jorge Salvador-Carlos *, Jimena Chairez-González, Ernesto Beltrán-Partida and Mario Curiel-Álvarez

Core Facility- Química y materiales avanzados, Instituto de Ingeniería, Universidad Autónoma de Baja California, Blvd. Benito Juárez and Normal s/n., 21280 Mexicali, Baja California, Mexico

* Correspondence: benval@uabc.edu.mx (B.V.-S.); jsalvador@uabc.edu.mx (J.S.-C.)

† These authors contributed equally to this work.

Abstract

Exposed bone fractures (EBF) represent a critical clinical challenge due to the simultaneous disruption of bone and surrounding soft tissues, requiring multifunctional biomaterials capable of providing mechanical adaptability, structural stability, and biological support. In this study, we developed a smart, shear-thinning, self-healing hydrogel composed of guar gum, polyvinyl alcohol, gelatin, collagen, and chitosan-stabilized manganese phosphate (MnP) micro/nanoparticles. MnP particles were synthesized via a quitosan/ascorbic acid-assisted route and characterized by SEM, DLS, FTIR, and EDS, confirming spherical morphology and successful phosphate incorporation. The resulting nanostructured hydrogel exhibited high porosity (>85%), controlled swelling, pH responsiveness, and efficient rheological self-recovery (>90% storage modulus restoration under cyclic deformation). The system demonstrated non-Newtonian behavior and effective adhesion to skin without irritation after 10 h of contact. In vitro assays using MC3T3-E1 pre-osteoblasts confirmed cytocompatibility and concentration-dependent modulation of cell migration. The incorporation of MnP micro/nanoparticles contributes potential osteogenic functionality while preserving mechanical integrity and dynamic responsiveness. These findings suggest that the developed nanocomposite hydrogel represents a promising auxiliary platform for the treatment of exposed bone fractures.

Keywords: stimuli-responsive biomaterial; multi-network; bone tissue engineering; osteoblast migration; skin biomaterials

1. Introduction

Bone tissue engineering (BTE) aims to restore structural integrity of damaged bone through biomaterials-based scaffolds capable of supporting cellular proliferation, differentiation, and extracellular matrix deposition [1,2]. However, in the case of exposed bone fractures (EBFs), the simultaneous disruption of bone and surrounding soft tissues creates a highly complex microenvironment characterized by inflammation, infection risk, mechanical instability, and impaired vascularization [3,4]. Although current clinical interventions such as fixation techniques, grafting procedures, and antimicrobial therapies are often effective, they still present limitations including incomplete regeneration, poor tissue integration, and insufficient modulation of the local biological response [5–7].

Smart hydrogels have emerged as promising candidates for BTE due to their three-dimensional hydrated networks, tunable mechanical properties, and capacity to incorporate bioactive agents [8–11]. Particularly, dynamic covalent and reversible physical crosslinking strategies enable injectability, self-healing capability, and responsiveness to environmental stimuli such as pH and temperature, making them particularly attractive for applications in dynamic wound environments [12–14]. These

 doi:10.20944/preprints202602.1380.v1

properties allow hydrogels to adapt to fluctuating physiological conditions while maintaining structural integrity and biological functionality.

For bone and skin applications, hydrogels must exhibit biocompatibility, osteoinductive potential, and mechanical resilience. Natural polymers such as guar gum (GG), gelatin (Gel), and collagen (Col), combined with synthetic polymers like polyvinyl alcohol (PVA), provide a versatile platform for constructing multifunctional networks [15–20]. Furthermore, the incorporation of nanostructured inorganic components within polymeric matrices has expanded hydrogel performance by introducing osteogenic stimulation and mechanical reinforcement.

Despite these advances, many currently available hydrogel systems still exhibit limited multifunctionality under the demanding physiological conditions associated with open fractures. Insufficient mechanical robustness, lack of adaptive responsiveness, and inadequate bioactivity restrict their translational potential, particularly in environments requiring simultaneous modulation of osteogenesis and angiogenesis [2,14].

Among trace elements involved in bone metabolism, manganese (Mn^{+2}) plays a critical role in osteogenic differentiation and extracellular matrix formation [21,22]. Manganese phosphate (MnP), when engineered at the micro/nanoscale, represents a promising yet underexplored strategy for enhancing osteoblastic activity while contributing to structural reinforcement of polymeric scaffolds [23–25]. However, the integration of MnP micro/nanoparticles within dynamic, self-healing hydrogel systems suitable for exposed fracture environments remains largely unexplored.

Therefore, this work proposes the development of a multifunctional GG/PVA-based hydrogel incorporating chitosan-stabilized MnP micro/nanoparticles. The aim is to generate a mechanically adaptive, stimuli-responsive and biologically active scaffold capable of supporting osteoblastic proliferation and migration while maintaining structural stability under physiologically relevant conditions.

2. Materials and Methods

2.1. Materials

The manganese chloride tetrahydrate ($MnCl_2{\cdot}4H_2O$), monopotassium phosphate (KH_2PO_4), 96% ethanol (EtOH) and polyvinyl alcohol (PVA) used, were from FAGALab, Mexicali, Mexico. Ascorbic acid (AA) from Fisher, Mexico. Hydrochloric acid (HCl) and ammonium hydroxide (NH_4OH) from Baker, Randor, PA, USA. Chitosan (CS) from Sigma Aldrich, Carlsbad, CA, USA. The guar gum (GG), vegetable glycerin (Gli), sodium borate (Bx) and hydrolyzed collagen (Col) from Cosmopolitan, CDMX, Mexico, tannic acid (TA) and n-Hexane from Jalmek, San Nicolás de los Garza, Nuevo León, Mexico, sodium hydroxide (NaOH) from Fermont, CDMX, Mexico and distilled water from Hwater, Mexicali, Mexico. A sterile PBS 1X pH 7.2 solution was prepared in our laboratory.

2.2. Synthesis of Micro/Nanoparticles of MnP

5 mL of a chitosan/ascorbic acid (CS/AA) solution with a 1:0.7 ratio was ultrasonicated (Branson 5800, CPX5800H, Emerson, Clayton, Missouri, USA, 22 kHz frequency at 40% amplitude, 200W) for 5 min, followed by the addition of 5 mL of a 0.025 M KH_2PO_4 solution and left to react for 10 min. Afterwards, 5 mL of a 0.0127 M $MnCl_2{\cdot}4H_2O$ solution was added dropwise and the reaction was continued for another 10 min. The solution was ultrasonicated in an ultrasonic homogenizer (OMNI SONIC RUPTOR 400, Omni International, Kennesaw GA, USA) at 30 kHz at 40% amplitude equipped with a sound control chamber for another 10 min, and the microparticles and nanoparticles were left in suspension.

2.3. Physicochemical Characterization of MnP Micro/Nanoparticles

Fourier transform infrared spectroscopy (FTIR, PerkinElmerFrontier, Waltham, MA, USA) was used to characterize the MnP. Each spectrum was measured over a wavenumber range of 4000 to 400 cm^{-1} with a resolution of 1 cm^{-1} [26]. The morphology, size and chemical composition were analyzed

 doi:10.20944/preprints202602.1380.v1

by using a scanning electron microscope (FE-SEM; LYRA 3, Tescan, Brno, Czech Republic) equipped with an energy dispersive X-ray (EDS, Tescan, Brno, Czech Republic) detector coupled to the SEM. The stability and size distribution of the NPs was evaluated using the Dynamic Light Scattering (Microtrac MRB Nanotrac Wave II; DLS, Duesseldorf, German) technique with a measurement range of 2-500 nm, at room temperature [27].

2.4. Hydrogel Synthesis

In order to synthesize the hydrogels, the GG and Gli were first mixed for 2 min to break up any lumps. Then, the necessary amount of water was added, immediately followed by adding the 4.28% *w/v* Gel solution and mixing until complete incorporation. Consequently, it was mixed with MnP (1000 ppm) in suspension in a CS/AA solution and the 1.4% *w/v* Col solution under constant stirring for 10 min. Next, a 1 N NaOH solution was added dropwise until the first color change was homogeneous throughout the solution. Then, the 4% *w/v* Bx solution was incorporated until the whole solution became transparent gray.

Then, TA was added slowly to avoid the generation of lumps and left stirring vigorously for 10 min until a homogeneous solution was obtained. The solution changed to a pinkish color, and finally, half of the 10% *w/v* PVA solution was slowly supplemented while stirring for 10 min, and the remaining half was incorporated and stirred very slowly to avoid air bubbles in the hydrogel. The final solution turned a pale pink color. The amount and order of incorporation of the reactants are shown in Table 1, while Figure 1 illustrates the preparation procedure.

Table 1. Components comprising each hydrogel with non-Newtonian fluid behavior developed in this study. Amounts in grams by mass and % *w/v*.

Name	*GG*		*Gli*		*Gel*		*MnP*		*Col*		*NaOH*		*Bx*		*TA*		*PVA*		*H₂O*	
Control	0.2	1%	2.39	18%	-	-	-	-	-	-	0.13	1%	2.6	19%	-	-	4.2	31%	4	30%
HD	0.2	1%	2.39	13%	3.07	16%	0.2	1%	0.75	4%	-	-	2.08	11%	0.1	1%	4.2	22%	6	32%

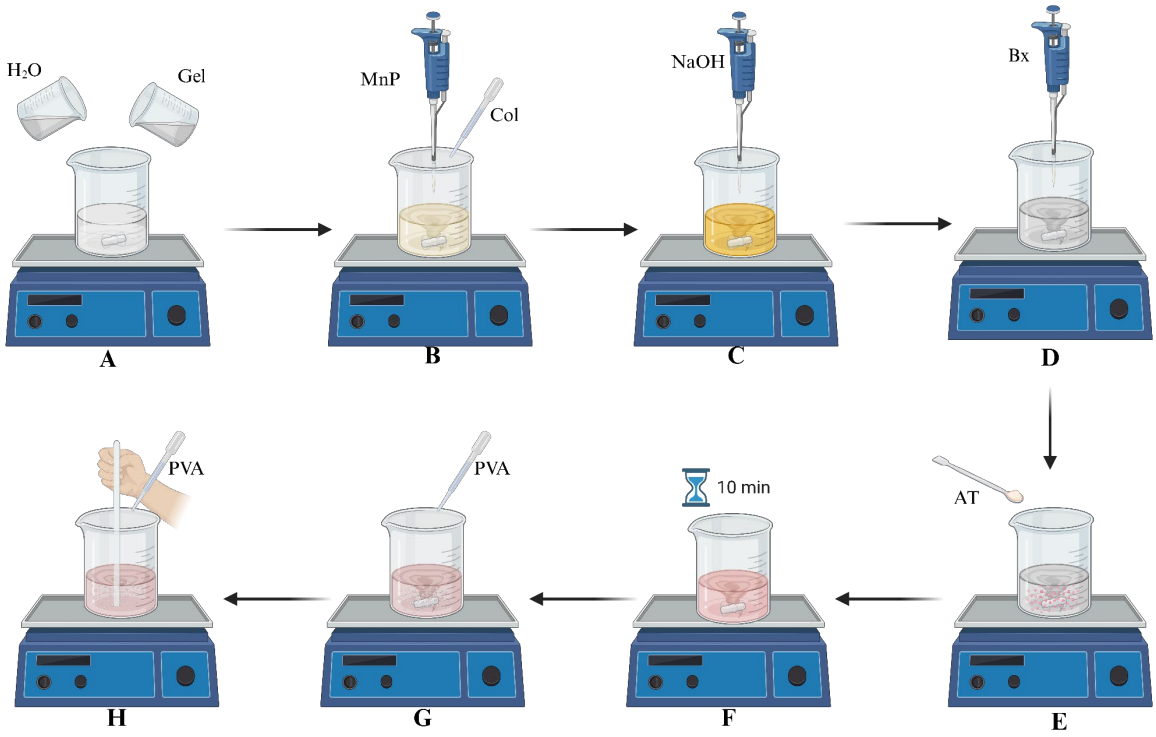

Figure 1. Procedure to obtain experimental hydrogels with non-Newtonian fluid behavior. A) Mixed GG, Gli and Gel, and finally water, B) Added MnP and Col, C) Added NaOH, D) Added Bx, E) Added AT slowly, F)

 doi:10.20944/preprints202602.1380.v1

Mixed for 10 min, G and H) Added PVA and agitated mechanical and manual form. Created with BioRender.com.

2.5. Hydrogel Characterization

2.5.1. Rheological Studies of Hydrogels

Rheological assessments were performed using a rheometer (Anton Parr MCR102, Anton Paar GmbH, Graz, Austria). Hydrogel disks with 25 mm diameter and 2.5 mm thickness were utilized to conduct frequency sweep, strain sweep and viscosity measurements. The frequency sweep (ω) ranged from 1 to 100 rad s^{-1}, allowing for the evaluation of changes in storage modulus (G′) and loss modulus (G′′). The amplitude sweep tested how G′ and G′′ responded to strains between 1-1000%, providing data on stress dependence and the yield strength of the hydrogels. All tests were performed three times.

2.5.2. Rheological and Self-Healing Performance

The ability of the hydrogel to repair itself after being cut was determined by longitudinally cutting one piece of the hydrogel into two parts. The two pieces were kept close together and were successfully assembled into one piece while retaining their original shape. It was then checked with contrary movements to see if the material still held together. This process was repeated using one drop of dye Green PGR7-L and Red ARE18 (Cosmopolitan, CDMX, Mexico) in one of the parts of the hydrogel, and the exact mechanism was observed [28,29] . In addition, the self-healing ability of the hydrogel was checked, for which a cut was made inside the surface of the hydrogels and shifted a little to each side to leave an empty space between them. The time it took to return to its original shape was observed and recorded when the cut made without the help of external stimuli disappeared [30]. The recovery and self-healing tests were conducted using a stereoscope (Leica, DMIL, Leica Microsystems, Wetzlar, Germany) with 40x magnification, and the rate of self-healing was measured by ImageJ (version 1.54g, National Institute of Health, Bethesda, MD, USA) software.

The rheological analysis of self-healing behavior of the hydrogels was evaluated by application of alternate amplitude sweep for five cycles each of 120 s at low 1% and high strains 1000% at a fixed frequency 6.28 rad s^{-1} [30]. The measurements were repeated three times.

2.5.3. Moisture Content

The hydrogels were then cut into 1×2 cm^2 pieces, weighted, placed in a desiccator for 5 days, and weighted once again. The percentage humidity content was calculated using the following equation [31]:

$$Humidity\ content(\%) = \left(\frac{W_1 - W_2}{W_1}\right) \times\ 100 \quad (1)$$

where W_1 is the initial weight, and W_2 is the weight of the dried sample. Measurements were performed in triplicate for each hydrogel.

2.5.4. Water Absorption Capacity

The hydrogels were cut into 1×2 cm^2 pieces, and their initial moisture content was measured. Subsequently, the samples were placed in a container with 4 mL of distilled water and left to soak for 3 h to prevent the gel from dissolving. Immediately, the samples were placed in a desiccator to remove surface moisture, and their final weight was measured. The absorbed moisture content was calculated using the following equation [31]:

$$Absorbed\ humidity\ content(\%) = \left(\frac{W_2 - W_1}{W_1}\right) \times\ 100 \quad (2)$$

where W_1 is the initial weight, and W_2 is the final weight. Measurements were performed in triplicate for each hydrogel.

 doi:10.20944/preprints202602.1380.v1

2.5.5. Porosity

The porosity of the hydrogels was measured by a slightly modified cyclohexane displacement method [32]. The hydrogels are immersed in 4 mL of cyclohexane after recording the weight of the empty container (W_1). The weight of the hydrogels before and after immersion in the cyclohexane were then recorded and designated as W_h and W_2, respectively. The hydrogel pores were filled with cyclohexane, and the volume of the cyclohexane in the hydrogel was considered to be the volume within the pores of the hydrogel. The measurement was replicated using 96% ethanol. The following formula was used to calculate the porosity:

$$V_h = \frac{W_h}{\rho_h} \quad (3)$$

$$V_p = \frac{W_2 - W_h - W_1}{\rho_s} \quad (4)$$

$$P = \frac{V_p}{V_p + V_h} \quad (5)$$

where V_h represents the hydrogel volume (mL), ρ_h y ρ_s is the density of the hydrogel and the solvent, respectively g mL^{-1} and V_p is the volume of the pore (mL). Each test was performed in triplicate.

2.5.6. Swelling Behavior in PBS

To measure the swelling behavior of the hydrogels, we followed the methodology reported by Perez-Diaz et al. [33] The pre-weighed hydrogels were immersed in 4 mL of PBS at room temperature. The absorbed PBS was measured at 30 min intervals for two hours with an analytical balance until equilibrium was reached. The PBS solution was removed and replaced with a new one in between measurements. The study was repeated at prolonged times of 4, 8, and 24 h. The swelling ratio of the hydrogels was estimated as follows:

$$Swelling\ degree\ (\%) = \frac{W_2 - W_1}{W_1} \times 100 \quad (6)$$

where W_2 is the wet hydrogel weight, and W_1 is the dried hydrogel weight. Measurements for each hydrogel were made in triplicate.

2.6. Hydrogel Characterization – External Stimuli

2.6.1. Hydrogel Behavior to External Stress Stimuli

The hydrogels were placed in 10 cm diameter Petri dishes, and two types of stresses were applied to them using a steel spatula. In the first stress, a minimal force (pressure ~ 1 kPa) was applied on the hydrogel surface for 2 s; consequently, the spatula was slowly lifted. The second effort was applying the same force as in the first stimulus but with the difference of being a fast stroke (<1s) on the hydrogel surface, and its behavior was observed.

2.6.2. Dissolution Behavior in Different Chemical Environments

0.5 g of each hydrogel was placed into 10 mL of distilled water, PBS, 70% *v/v* EtOH solution, 1 N HCl, and 1 N NaOH, separately for 1 day, and the presence of solid-gel material was observed within the containers.

The dissolution of the hydrogels was estimated as follows:

$$Dissolution\ (\%) = \frac{W_2 - W_1}{W_1} \times 100 \quad (7)$$

where W_2 is the original hydrogel weight, and W_1 is the hydrogel weight remain before filter with Whatman #1. Measurements for each hydrogel were made in triplicate.

2.6.3. Adhesion and Surface Interaction Behavior

 doi:10.20944/preprints202602.1380.v1

The method proposed by X. Su et al. [34] was followed with slight modifications. A small sample of each hydrogel was taken and subjected to contact with various surfaces (paper, cardboard, aluminum, silicone, fabric, rubber, plastic, and human skin) to check the adhesion capacity at standard temperature and pressure conditions. In addition, peel/stick tests were carried out on human skin for several cycles, as well as push-ups and movements. Finally, the hydrogels were placed on the skin for 10 h to simultaneously observe the effect on the skin and the changes in the hydrogel.

2.6.4. Wettability

To evaluate the moisturizer of the hydrogels, the contact angle between the surface of the hydrogel and a drop of ultrapure water was monitored. A flat piece of the hydrogel was fixed on a glass holder, then a drop of 16 µL of ultrapure water on the hydrogel was placed with the help of a syringe and the image was taken after 2 s at room temperature. All hydrogels contact angles were measured by triplicate.

2.6.5. Water Adhesion

A small hydrogel sample was taken and introduced into 20 mL of water at room temperature without any additional treatment [34]. Subsequently, the hydrogel was pressed with a fingertip (pressure ~ 1 kPa) for 10 s, and then the external pressure was removed immediately to observe its adherence capacity. The experiment was repeated, but the hydrogel was pressed outside of water. Once adhered, it was introduced into water, and it was observed if the hydrogel detached.

2.6.6. Temperature Responsiveness

Using 2 mL of each hydrogel, they were exposed to a water bath with gradual and controlled heating (1 °C min^{-1}). After reaching 40 °C, the hydrogels were slightly stirred and placed upside down to observe if they flowed. This procedure was repeated each time the temperature was increased by one degree. The measurement was concluded once the hydrogels were observed to flow. Likewise, the hydrogels were exposed to decreasing temperatures under a minimum temperature of −20 °C. Once the minimum temperature was reached, the two hydrogels were frozen and removed from the cold environment. The temperature was monitored while attempting to pierce the hydrogels lightly with a wooden stick. Once the hydrogels could be pierced, the temperature was taken as the maximum temperature to withstand before freezing.

2.6.7. pH Responsiveness

Solutions of 1 N HCl and 1 N NaOH were added dropwise by separating a sample of each hydrogel to check its gelation at different pH conditions. In addition, 0.5 g of the hydrogels were left for 48 h in three buffer solutions at pH 4.01, 7.0, and 10.01 to observe the changes in the hydrogel.

2.7. Biological Tests

2.7.1. Cell Culture

The mouse embryonic calvary cell line (MC3T3-E1) was purchased from ATCC CRL-2594 (Manassas, VA, USA). Cells were cultured in α-minimum essential medium (α-MEM, Gibco, Invitrogen, Waltham, MA, USA) supplemented with 10% heat-inactivated FBS (Gibco, Invitrogen) and 1% penicillin (100 Um L^{-1}) and streptomycin (100 µg mL^{-1}) (Gibco, Invitrogen, Waltham, MA, USA). The cells were incubated at 37 °C in a humidified atmosphere containing 5% CO_2 until 80% confluence was reached.

2.7.2. MTT Assay for Cell Viability

 doi:10.20944/preprints202602.1380.v1

In order to evaluate the cytotoxic activity of the experimental biopolymers, we use the (3-(4,5-dimethylthiazol-2-yl)-2,5-diphenyl tetrazolium bromide (MTT) viability assay. Initially, 15,000 cells mL^{-1} of MC3T3-E1 were incubated in each well of a 96-well plate (Corning, New York, NY, USA) with 100 µL of each 10% and 5% hydrogel in triplicate for 24h. The culture medium was removed with special care to keep the monolayer of cells formed intact. The cells were washed with warm PBS for 5 min. Then, 200 µL of MTT solution (5 mg mL^{-1}, Sigma Aldrich, Carlsbad, CA, USA) was added to each well and incubated at 37 °C in a humidified incubator with 5% CO_2 for 3 h. The resulting formazan crystals were dissolved after discarding the MTT-containing medium, and the 96-well plate was transferred to an orbital shaker at 200 rpm and 37 °C, with 200 µL of dimethyl sulfoxide (Sigma Aldrich, Carlsbad, CA, USA) for 20 min under dark conditions. Then, the optical density (OD) was measured at 590 nm with a microplate reader (Thermoskan, Thermo Fisher Scientific, Carlsbad, CA, USA). The baseline control was performed using a culture medium prepared for MTT without MCET3-E1, and cells only with the complete medium were used as a negative cytotoxicity control [35].

2.7.3. Scratch Test

The MC3T3-E1 cells were seeded at 25 × 10^3 cells $well^{-1}$ in individual wells of sterile 12-well culture plates (Corning, New York, NY, USA) and incubated until a confluent monolayer (100%) was obtained. The monolayer was then washed thrice with warm PBS, and a wound was generated using a sterile 20 – 200 µL tip by sliding the tip along the cell surface in the direction of 12 to 6 according to clockwise [36]. The wells were then washed with warm PBS to remove any cell debris, and the cells were cultured with α-MEM (5% FBS, control) or α-MEM (5% FBS) supplemented with the hydrogels (1.56%, 3.125%, 6.25% and 12.5%). Wound closure was monitored at baseline and after 24h of treatment using a digital phase contrast microscope (ZOE, Bio-Rad, Irvine, CA, USA). Finally, an MTT assay was applied (following the previously established procedure) to monitor cell activity during the wound repair process after 24h of treatment.

2.8. Statistical Analysis

Numerical data were analyzed after three independent studies, each conducted in triplicate. Results were expressed as the mean ± standard deviation and evaluated using GraphPad Prism 9 (GraphPad Software Inc., San Diego, CA, USA). Significances were determined by comparing one-way analysis of variance (ANOVA) followed by Tuckey's multiple comparisons test. Differences were considered statistically significant at a $p<0.05$ level.

3. Results

3.1. Physicochemical Characterization of MnP Micro/Nanoparticles

Stable yellow to opaque-yellow colloidal suspensions of MnP micro/nanoparticles were successfully obtained through the CS/AA-assisted synthesis route. SEM analysis (Figure 2a) revealed the formation of spherical to quasi-spherical particles embedded within the CS matrix. At higher magnification, discrete domains corresponding to MnP particles were clearly distinguished from the polymeric background, with an estimated average diameter of approximately 232 ± 70 nm (measured from SEM micrographs). The surrounding CS network acts as both a nucleation template and a stabilizing agent, preventing uncontrolled particle growth and aggregation.

The DLS analysis (Figure 2b) revealed a multimodal size distribution with a Z-average (Mz) of 160 nm. The median particle diameter (D50) was 30.7 nm, indicating a significant nanoscale fraction. Approximately 80% of the particle population was below 398 nm, while larger micrometric fractions correspond to secondary aggregation phenomena, as confirmed by the volume-weighted distribution. The broad distribution profile reflects the presence of CS/AA-stabilized MnP nanoparticles coexisting with polymer-associated clusters. On the other hand, the zeta potential was

 doi:10.20944/preprints202602.1380.v1

−200 mV indicates a highly stable colloidal system due to strong electrostatic repulsion mediated by protonated CS a phosphate groups (conductivity of 1.55 mS cm^{-1}).

The results of the EDS analysis confirmed the presence of Mn (30.62%), P (10.91%), O (43.68%), and C (9.46%) and small traces of other elements belonging to residues and non-reacting reagents (Figure 2c). The Mn:P ratio is consistent with the formation of manganese phosphate phases, while the high oxygen content reflects both phosphate groups and hydroxyl functionalities from the CS matrix. The carbon signal originates from the polysaccharide backbone, confirming the successful integration of the inorganic phase within the polymeric stabilizing medium.

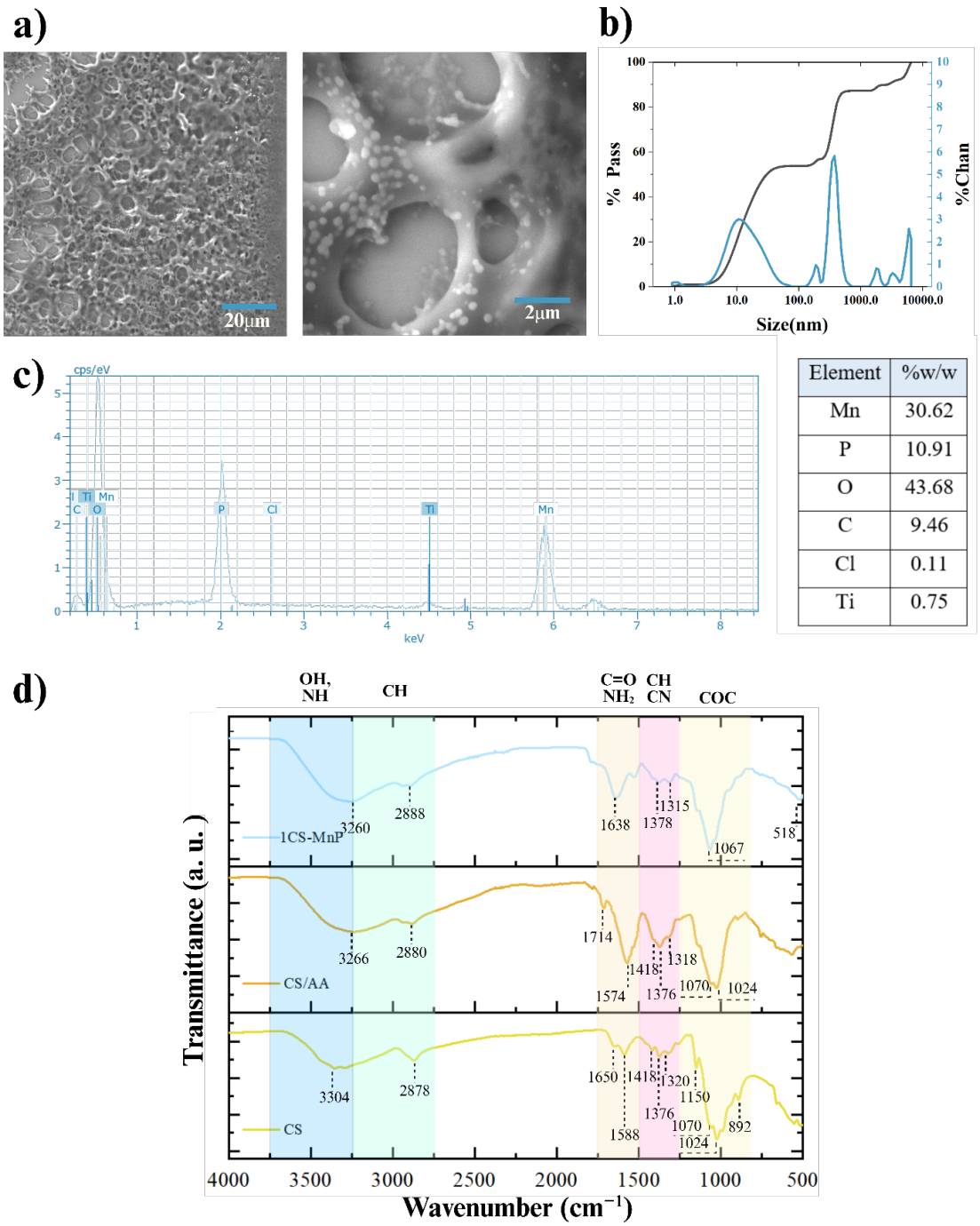

Figure 2. a) SEM images of the CS–MnP nanocomposite showing a porous chitosan matrix with embedded MnP particles, b) particle size distribution by DLS analysis; c) EDS elemental composition (Mn, P, O); and d) FTIR spectra highlighting interactions between chitosan functional groups and phosphate species.

 doi:10.20944/preprints202602.1380.v1

The FTIR spectra corresponding to the CS/AA-assisted synthesis are presented in Figure 2d. The spectra of CS and CS/AA exhibit the characteristic absorption bands of CS [37]. Broad bands at 3304 cm^{-1} and 3266 cm^{-1} are attributed to the overlapping vibrations of N−H and O−H groups. The peaks at 2878 cm^{-1} and 2880 cm^{-1} correspond to C−H stretching vibrations. In the case of CS, the band observed at 1650 cm^{-1} is assigned to the C=O stretching of amide groups and the bending vibration of NH_2.

Additional bands at 1418 cm^{-1}, 1376 cm^{-1} and at 1320 cm^{-1}, associated with C−H bending vibrations, while the peak at 1318 cm^{-1} corresponds to −C−N stretching. The bands located at 1070 cm^{-1} and 1024 cm^{-1} are attributed to C−O vibrations [38]. Furthermore, CS presents characteristic peaks at 1150 cm^{-1} and 892 cm^{-1} related to C−O−C vibrations of the polysaccharide backbone. In contrast, CS/AA shows increased intensity at 1574 cm^{-1}, which is associated with C=C stretching, along with enhanced protonation of amino groups (NH_3^+) due to the presence of AA. The appearance of a band at 1714 cm^{-1} confirms the presence of carboxyl acid groups from AA [38,39]

On the other hand, the MnP spectrum displays a pronounced band showed an intense at 1067 cm^{-1} due to the presence of phosphate vibrations overlapping with C−O contributions [40]. A noticeable shift and decrease in intensity of the peak corresponding to C=O and NH_2 at 1638 and 1510 cm^{-1}, respectively, suggest interactions between MnP and the functional groups of CS. Compared with the CS/AA spectrum, this attenuation indicated that the microparticles interact with protonated NH_3^+ groups of CS in solution, which reduces their spectral intensity. Likewise, the peaks at 2888 cm^{-1} and 3260 cm^{-1} are attributed to O−H and N−H and at 1378 cm^{-1} and 1315 cm^{-1} to possible C−H and C−N groups which were also present in the CS and CS/AA spectra. Finally, the peak at 518 cm^{-1} corresponds to O−P−O bending vibrations, confirming the presence of phosphate structures [41,42].

3.2. Hydrogel Characterization

3.2.1. Synthesis

The developed hydrogels exhibited distinct physicochemical changes during synthesis, particularly color transitions associated with progressive crosslinking steps (Figure 3a). The initial formulation promoted electrostatic interactions between protonated amine groups (NH_3^+) from CS/AA-stabilized MnP particles and carboxylate groups (COO^-) groups from Gel and Col, generating a preliminary physically crosslinked network (Figure 3b$_1$) [43]. Additionally, Mn^{+2} and PO_4^{-3} ions contributed to ionic coordination within the polymeric matrix, acting as secondary crosslinking sites and enhancing structural cohesion [44,45].

The GG, on the other hand, significantly increased the apparent viscosity due to its high hydroxyl content, promoting hydrogen bonding interactions within the matrix [46,47]. In contrast, Gli acted as a plasticizer by interacting with hydroxyl groups of GG, PVA, and peptide chains, increasing chain mobility while preserving network continuity [48].

Upon NaOH addition, Bx hydrolysis generated tetrahydroxyborate ions ($B(OH)_4^-$), which formed reversible diol-borate ester bonds with GG and PVA hydroxyl groups (Equations 8 and 9). This step introduced a dynamic covalent network (Figure 3b$_2$), responsible for the hydrogel's adaptive mechanical behavior. The observed color shift to pale gray corresponded to pH adjustment and borate complex formation [46,49,50].

$$2Na_2B_4O_7 \cdot 10H_2O + 4H_2O \rightarrow 4B(OH)_3 + 4B(OH)_4^- + 4Na^+ \quad (8)$$

$$4B(OH)_3 + 2H_2O \leftrightarrow 3B(OH)_3 + B(OH)_4^- + H_3O^+ \quad (9)$$

The incorporation of TA further reinforced the structure through hydrogen bonding and possible Schiff-base interactions with amino groups from Gel and Col [51]. Controlled oxidation of catechol groups under mildly alkaline conditions contributed to additional dynamic crosslinking without compromising biocompatibility [52,53]. The solution changed color to a pale pink-orange.

Finally, PVA integration allowed the formation of borate ester linkages between adjacent chains, establishing a multi-network hydrogel system (Figure 3b$_3$) [54]. Importantly, the synthesis did not

 doi:10.20944/preprints202602.1380.v1

require freeze-thaw cycles typically employed in PVA-based hydrogels, demonstrating a milder and potentially scalable fabrication strategy [55].

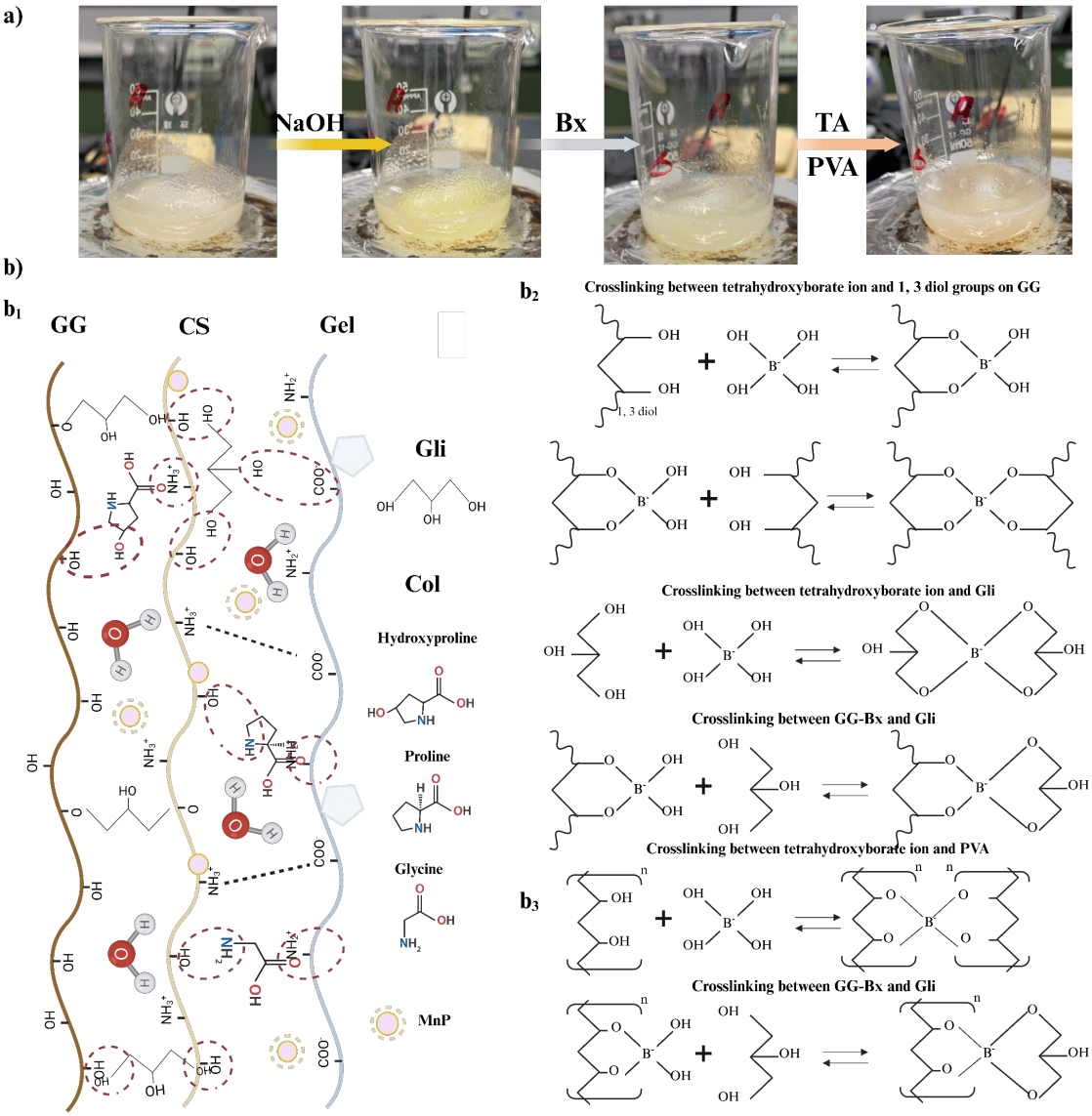

Figure 3. a) Phases of the hydrogel and their color changes due to the addition of specific reagents. b) Possible interactions within the hydrogel; b_1) Electrostatic interactions between the base formulation consisting of the first compounds between the NH_3^+ and C=O, COO^- and OH groups, as well as hydrogen bonds. b_2) Cross-linking mechanism between the tetrahydroxyborate ion from Bx in an aqueous medium, forming monodiol complexes at first, followed by the adjacent formation of another diol with GG and Gli, as well as between themselves (GG-Bx-Gli). b_3) Cross-linking mechanism between the tetrahydroxyborate ion and PVA, as well as with Gli (PVA-Bx-Gli). Created with BioRender.com.

3.2.2. Rheological Studies: Frequency Sweep

The rheological behavior of the developed hydrogels was evaluated through oscillatory frequency sweep measurements (Figure 4a,b). The Control hydrogel exhibited two crossover point between the storage modulus (G′) and the loss modulus (G″), where G″>G′, indicating dominant viscous behavior within specific frequency ranges and reduced structural stability. The relatively small gap between G′ and G″ suggests a weakly structured network susceptible to transition between elastic and viscous responses [56,57].

 doi:10.20944/preprints202602.1380.v1

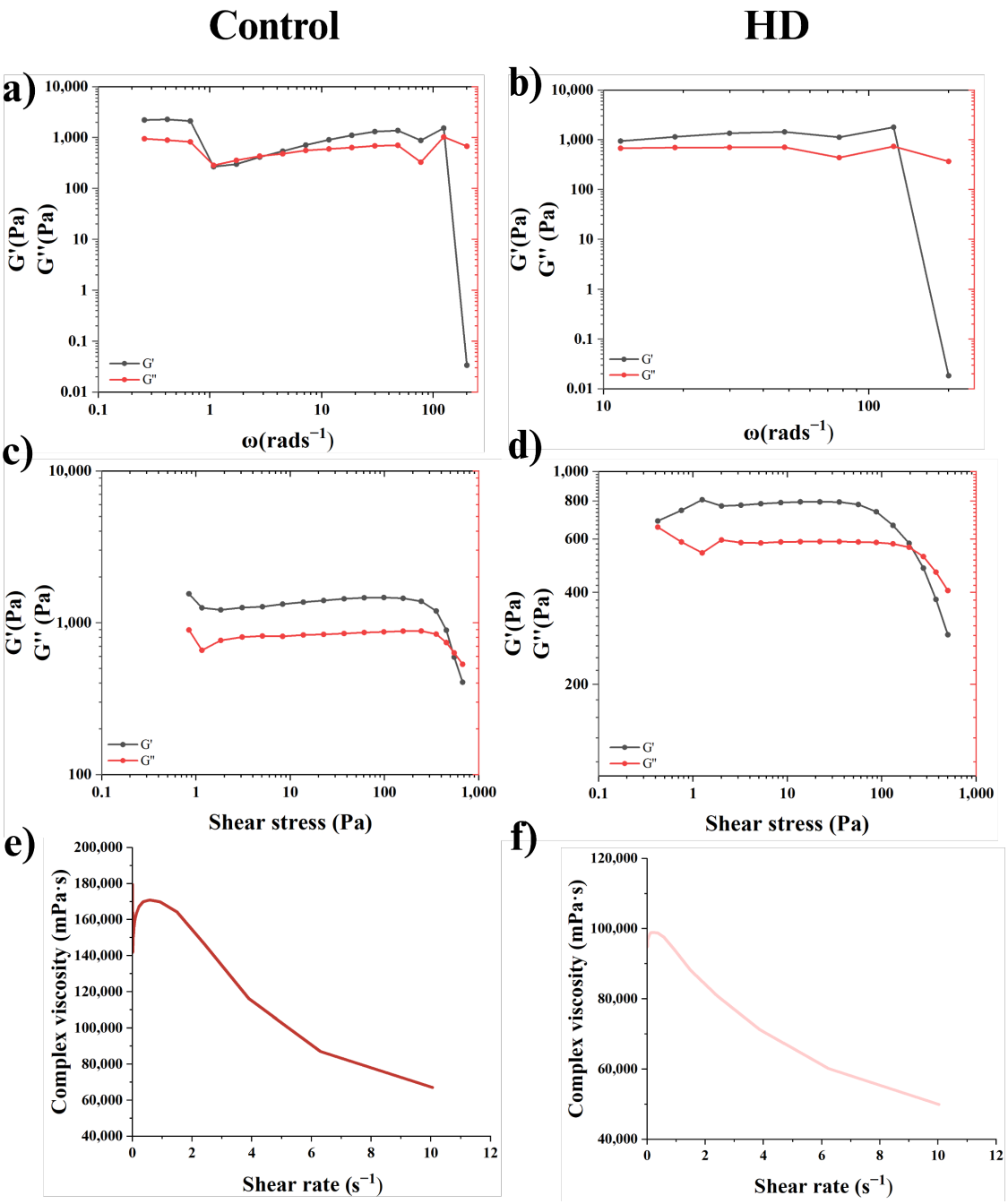

Figure 4. Rheological tests of the developed hydrogels. a) and b) Storage Modulus (G′) / Loss Modulus (G″) vs Control and HD frequency; c) and d) G′/G″ vs sheer force of Control and HD; e) and f) complex viscosity vs shear rate of Control and HD.

In contrast, the HD hydrogel displayed a predominantly elastic response across the investigated frequency range, with G′ consistently higher than G″. This frequency-dependent behavior indicates the formation of a stable and well-organized multi-network structure. The solid-liquid transition occurred at a higher angular frequency (~129 rad s^{-1}), with a corresponding modulus of 700.64 Pa, suggesting stronger intermolecular interactions and improved structural integrity. The dominance of G′ over G″ confirms that elastic contributions prevail, consistent with a dynamically crosslinked system governed by reversible borate-diol interactions and ionic coordination [58].

3.2.3. Rheological Studies: Deformation Sweep

The strain sweep analysis (Figure 4c,d) revealed a well-defined linear viscoelastic region (LVR) for both hydrogels, characterized by constant G′ and G″ values at low strain amplitudes. Within this

 doi:10.20944/preprints202602.1380.v1

region, the internal network remains structurally intact. Beyond the critical strain, a progressive decrease in G′ accompanied by an increase in G′′ indicates structural breakdown and yielding of the network [58,59].

The Control hydrogel exhibited a broader LVR and higher yield stress (γ) (667.66 Pa) compared to HD hydrogel (572.13 Pa), suggesting a more rigid and deformation-resistant structure. Conversely, the HD hydrogel showed earlier network yielding, consistent with increased flexibility due to its dynamic crosslinking architecture. This behavior reflects the balance between mechanical strength and adaptability introduced by the multi-network design.

3.2.4. Rheological Studies: Viscosity and Behavior Identification

The complex viscosity ($\dot{\eta}$) as a function of shear rate is presented in Figure 4e,f. Both hydrogels demonstrated pronounced shear-thinning behavior, evidenced by a progressive decrease in viscosity with increasing shear rate. At low shear rates, the high viscosity values indicate strong intermolecular interactions and polymer chain entanglement. As shear rate increases, the alignment of polymers chains and reversible disruption of physical crosslinks result in reduced resistance to flow. In both systems, the viscosity decreases progressively with increasing shear rate, clearly indicating a non-Newtonian shear-thinning behavior [57,60].

The Control hydrogel exhibited consistently higher viscosity values across the entire shear rate, indicating a denser and more rigid network. In contrast, the HD hydrogel showed lower viscosity and enhanced flowability, suggesting improved processability under applied shear [61]. This combination of structural stability at rest and flowability under stress is advantageous for potential biomedical applications requiring injectability or conformal adaptation to irregular defect geometries.

3.2.5. Rheological and Self-Healing Performance

The self-healing capacity of the hydrogels was first evaluated trough macroscopic cutting experiments (Figure 5a). After longitudinally dividing the samples into two separate parts, both Control and HD hydrogels exhibited spontaneous adhesion upon recontact without the application of external stimuli. Dye-assisted experiments confirmed effective interfacial fusion, indicating rapid reformation of dynamic bonds across the cut interface (Video S1).

The HD hydrogel demonstrated complete structural reconnection within 40-90 s, with an estimated healing rate of 0.0016 $cm^2\ s^{-1}$. This range is due to the effect of air bubbles, which can indeed influence the self-healing capabilities of the material by creating zones of lower density. These areas may reduce the elastic modulus and, consequently, diminish effective self-repairing ability. Nevertheless, our results remain strong, as HD demonstrated excellent recovery, achieving immediate restoration and complete self-healing within 90 s. By comparison, the self-recovery rate of hydrogels crosslinked with borax, PVA, and TA varies from minutes to hours, such as in the Control hydrogel (~3 min) and previous studies of hydrogel self-recovery [30,62,63].

On the other hand, dynamic self-healing behavior was further validated by oscillatory step-strain measurements (Figure 5b). Alternating low (1%) and high (1000%) strain cycles were applied for five consecutive intervals to simulate mechanical disruption and recovery.

Upon application of high strain, a pronounced drop in the G′ of nearly three orders of magnitude was observed, accompanied by convergence toward the G′′, indicating temporary breakdown of the three-dimensional network. When the strain was reduced back to 1%, both hydrogels rapidly recovered their elastic modulus, confirming reversible crosslinking behavior.

The HD hydrogel exhibited highly consistent modulus recovery across successive cycles, recovering approximately 90-95% of its initial G′ value after each deformation event. In contrast, although the Control hydrogel displayed slightly higher initial G′ values, it showed comparatively greater fluctuation during repeated cycles, suggesting a less dynamically adaptive structure.

 doi:10.20944/preprints202602.1380.v1

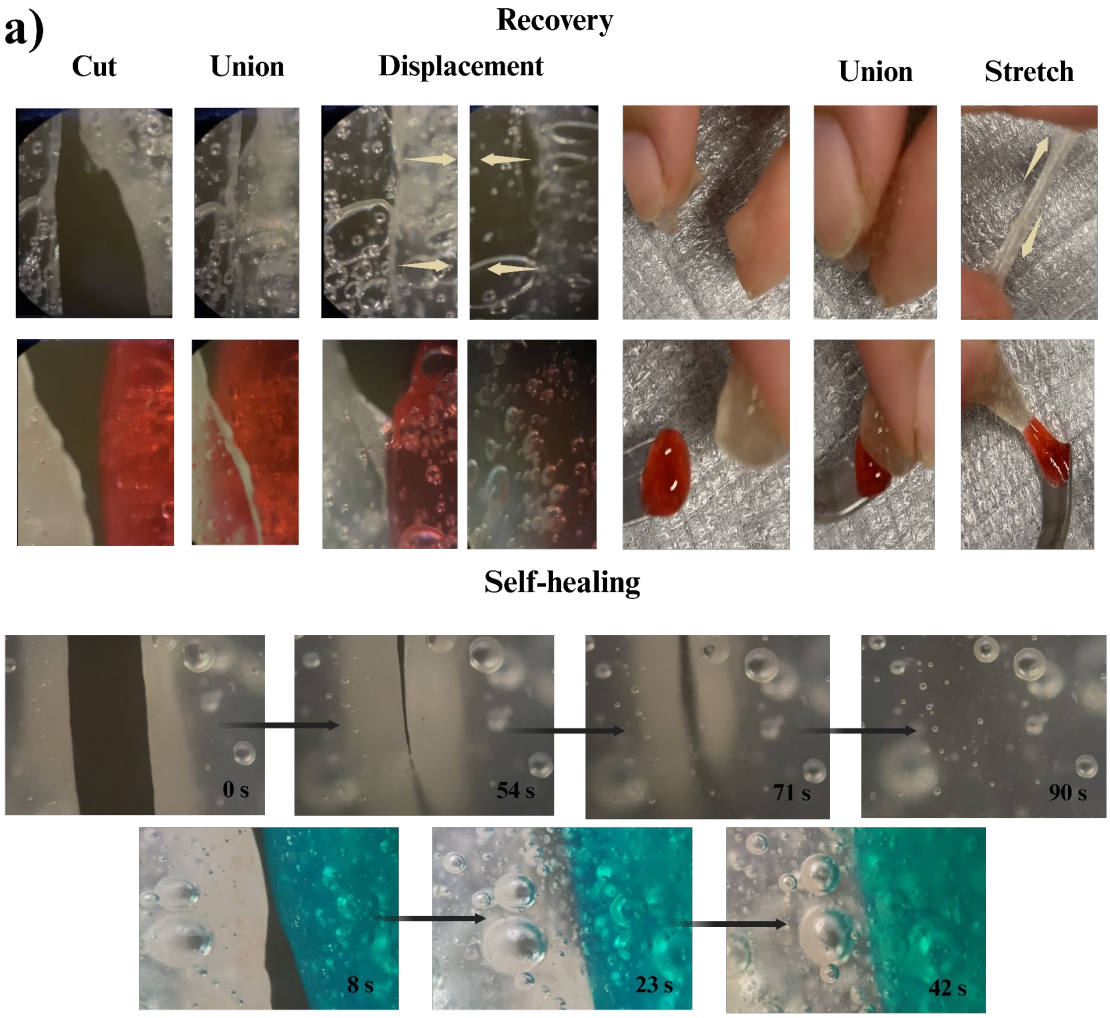

Figure 5. a) Evidence of recovery capacity when subjecting the hydrogel to cuts or separation of pieces in order to return to contact. The arrows show the displacement and stretching caused in the hydrogel, while maintaining its recovered bonds. Optical microscopy was used to observe the self-healing process of the hydrogel crack. b) Rheological evaluation of restructuring of hydrogels by subjecting alternate low (1%) and high (1000%) strains for five cycles.

The reversible dissociation and reformation of borate-diol (O–B–O) linkages, combined with hydrogen bonding interactions among PVA, Gli, TA, and polysaccharide chains, are primarily responsible for the observed recovery behavior [64]. Additionally, minor ionic coordination mediated

 doi:10.20944/preprints202602.1380.v1

by MnP particles contributes to network stabilization without compromising dynamic mobility [65,66].

Overall, the integration of dynamic covalent bonds, ionic interactions, and hydrogen bonding results in a mechanically resilient and self-adaptive hydrogel capable of dissipating mechanical energy and rapidly reorganizing its internal structure after deformation. This behavior supports its suitability for applications requiring structural adaptability under repetitive mechanical stress.

In applications for the repair of bone defects, it is attractive that the hydrogel can regenerate by itself, as it would allow the patient to apply it as many times as necessary to fill the wound or cover the damaged area. Moreover, in scenarios involving impacts or injuries to the hydrogel itself, it could return to its original state, sealing or recovering its integrity without losing the shape of the defect to be regenerated.

3.2.6. Moisture Content

The intrinsic moisture content of the hydrogels was determined after storage in a desiccator for 5 days (Figure 6a). Both formulations exhibited high water retention, with values of 81.61% for HD and 81.57% for the Control hydrogel. These nearly identical values indicate that the incorporation of MnP micro/nanoparticles does not significantly alter the overall water content of the polymeric matrix. The corresponding solid fraction accounted for approximately 18.4% of the total mass in both systems, confirming a highly hydrated network characteristic of soft hydrogel structures.

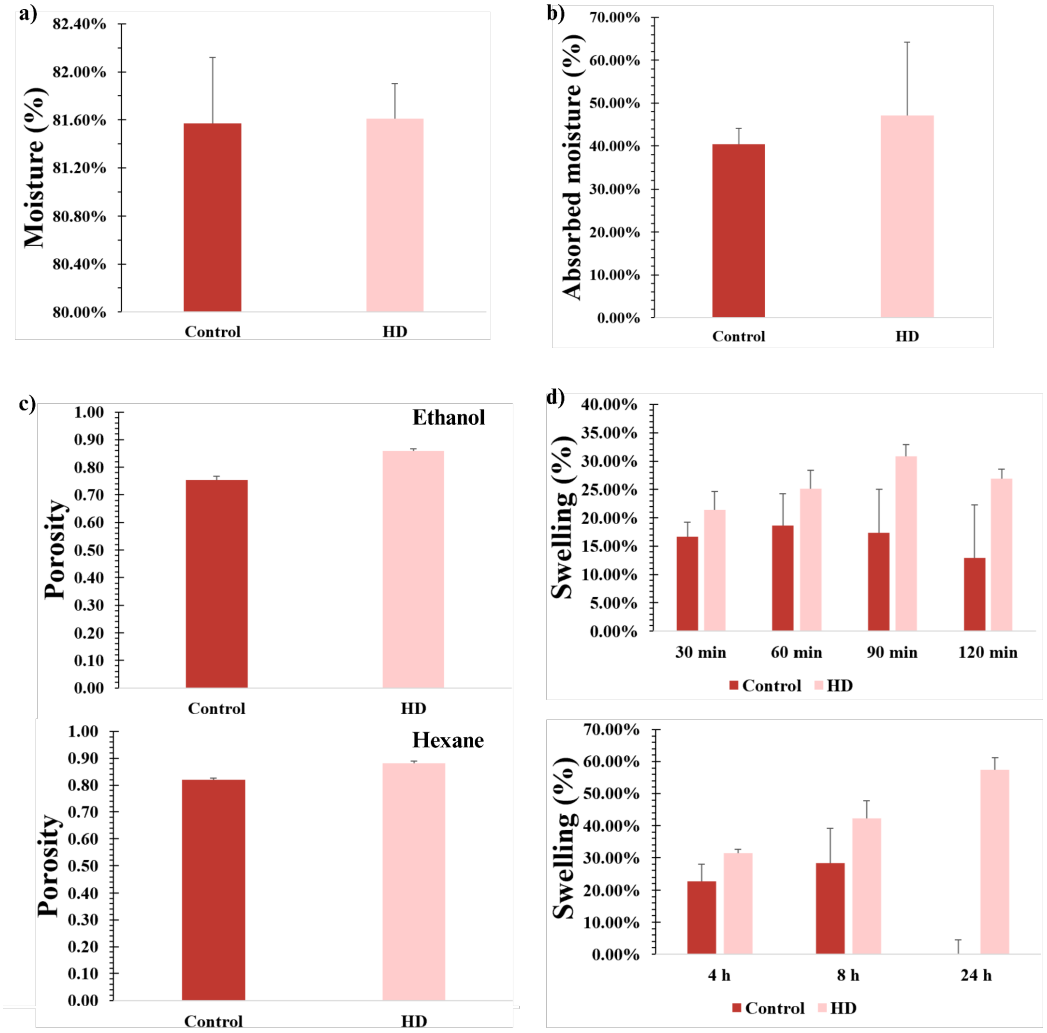

Figure 6. a) Analysis of the moisture content of each hydrogel; b) Water absorption capacity of the studied hydrogels; c) Porosity of the hydrogels, carried out in both 96% ethanol and hexane, showing a high degree of

 doi:10.20944/preprints202602.1380.v1

similarity between the results; d) Swelling capacity of the hydrogels using a PBS solution at different times. Data are presented as mean ± SD, n=3.

3.2.7. Water Absorption Capacity

The maximum water absorption capacity prior to structural collapse is shown in Figure 6b. The HD hydrogel exhibited a higher absorption limit (47.16%) compared to the Control (40.38%). This enhanced water uptake is attributed to the presence of additional free functional groups and the multi-network architecture, which promote hydrogen bonding interactions with water molecules while maintaining structural integrity [31].

The higher absorption threshold observed in HD suggests improved network flexibility and stability under swelling conditions. In contrast, the lower absorption capacity of the Control hydrogel may be associated with increased osmotic effects resulting from residual borate species, which could accelerate structural weakening under excessive hydration [46].

The results indicate that MnP particles incorporation and dynamic crosslinking contribute to improved swelling tolerance without compromising network stability.

3.2.8. Porosity

The porosity values of the hydrogels are presented in Figure 6c. The HD hydrogel exhibited porosity values of 0.8583 (ethanol) and 0.8820 (hexane), whereas the Control hydrogel showed lower values of 0.7531 (ethanol) and 0.8195 (hexane). These results indicate a highly porous structure in both systems, with a consistently higher porosity in the HD formulation.

The increased porosity in HD correlates with its enhanced water absorption capacity, facilitating capillary-driven liquid diffusion within the three-dimensional network. Despite both hydrogels displaying interconnected pore structures, the HD hydrogel demonstrated greater structural uniformity, suggesting a more homogeneous multi-network architecture. On the other hand, the comparatively lower porosity of the Control hydrogel may reflect a less uniform pore distribution, which can limit fluid transport under swelling conditions.

An adequate pore size distribution is an attractive feature to promote and control bone and dermal regeneration. This is because cells can adhere to the hydrogel surface and within the hydrogel, providing adequate structural support with a natural tissue environment, allowing the cells to differentiate, mature, and proliferate faster [8,67,68].

3.2.9. Swelling Behavior in PBS

The swelling behavior of the hydrogels was evaluated in PBS over time (Figure 6d). During the initial 2 h (measured at 30 min intervals), the HD hydrogel exhibited moderate swelling, reaching values of 3.74% and 5.64% in the early stages. After this period, slight structural relaxation was observed, eventually leading to the appearance of the first microcracks under continuous exposure.

In extended time measurements, HD maintained structural integrity and exhibited a gradual increase in swelling percentage, reaching higher equilibrium values compared to short-interval measurements. The swelling progression remained relatively stable over 24 h, suggesting controlled fluid uptake without premature structural collapse.

In contrast, the Control hydrogel exhibited rapid initial swelling between 30 and 60 min (18.62%), followed by a progressive decrease associated with network destabilization. Although a maximum swelling value of 28.23% was observed at 8 h, structural collapse occurred before 24 h, indicating reduced stability under physiological saline conditions.

The reduced swelling observed in PBS compared to distilled water can be attributed to ionic screening effect and decreased osmotic pressure in saline environments, which limit polymer expansion [69]. Overall, the HD hydrogel demonstrated improved swelling tolerance and structural resilience under physiologically relevant conditions.

3.3. Hydrogel Characterization – External Stimuli

 doi:10.20944/preprints202602.1380.v1

3.3.1. Hydrogel Behavior to External Stress Stimuli

The mechanical adaptability of the hydrogels was qualitatively evaluated under slow and rapid mechanical stress (Figure 7, Video S2). Under slow, minimal force, both formulations exhibited adhesive and extensible behavior. The HD hydrogel demonstrated pronounced elongation while maintaining structural continuity, indicating effective reversible bond rearrangement within the multi-network system. In contrast, the Control Hydrogel showed limited extensibility, suggesting a comparatively less dynamic internal structure.

When subjected to rapid and intense stress, both hydrogels exhibited solid-like behavior, resisting flow and detaching from contact surfaces. This dual response is consistent with the previously observed viscoelastic and shear-thinning properties (non-Newtonian). The ability of HD to stretch under low stress while resisting rapid deformation suggests a network dominated by reversible borate-diol interactions and hydrogen bonding, which allow stress dissipation without permanent structural damage. Similar stress-responsive behavior has been reported in dynamic borate-crosslinked systems, where bond exchange kinetics govern adaptability [70].

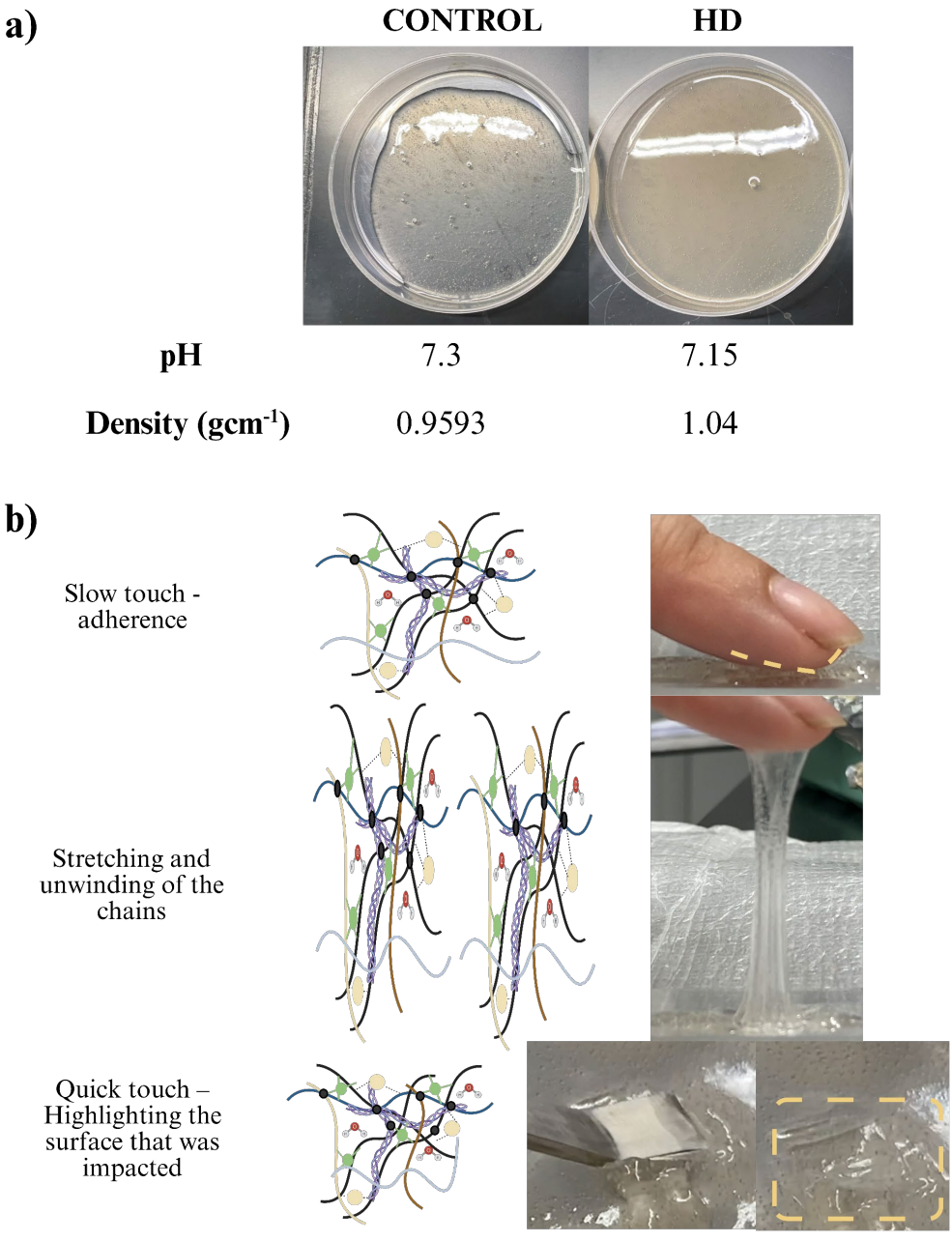

 doi:10.20944/preprints202602.1380.v1

Figure 7. a) Hydrogels with their respective pH values and obtained densities. b) Behavior of the non-Newtonian hydrogel, since under low-energy stresses it behaves like a fluid and easily adheres to the surface, but under a quick touch, considering a bigger energy stress, the hydrogel behaves like a solid. Created with BioRender.com.

3.3.2. Dissolution Behavior in Different Chemical Environments

The dissolution performance was assessed after 24 h immersion in distilled water, PBS, 1N HCl, 1 N NaOH, and 70% v/v EtOH solution (Figure 8). In distilled water, both hydrogels exhibited substantial dissolution, consistent with their high swelling capacity under low ionic strength conditions. In PBS, the Control hydrogel showed similar behavior, whereas HD maintained structural integrity with moderate swelling, reflecting improved resistance under physiological saline conditions.

Under strongly acidic conditions, significant destabilization occurred. The Control hydrogel completely dissolved, while HD retained partial integrity (88.20% dissolution). Acidic environments likely disrupt electrostatic interactions and weaken hydrogen bonds by protonating amino and carboxyl groups, leading to network collapse [69,71]. The comparatively lower dissolution of HD suggests that its multi-network structure provides additional stabilization.

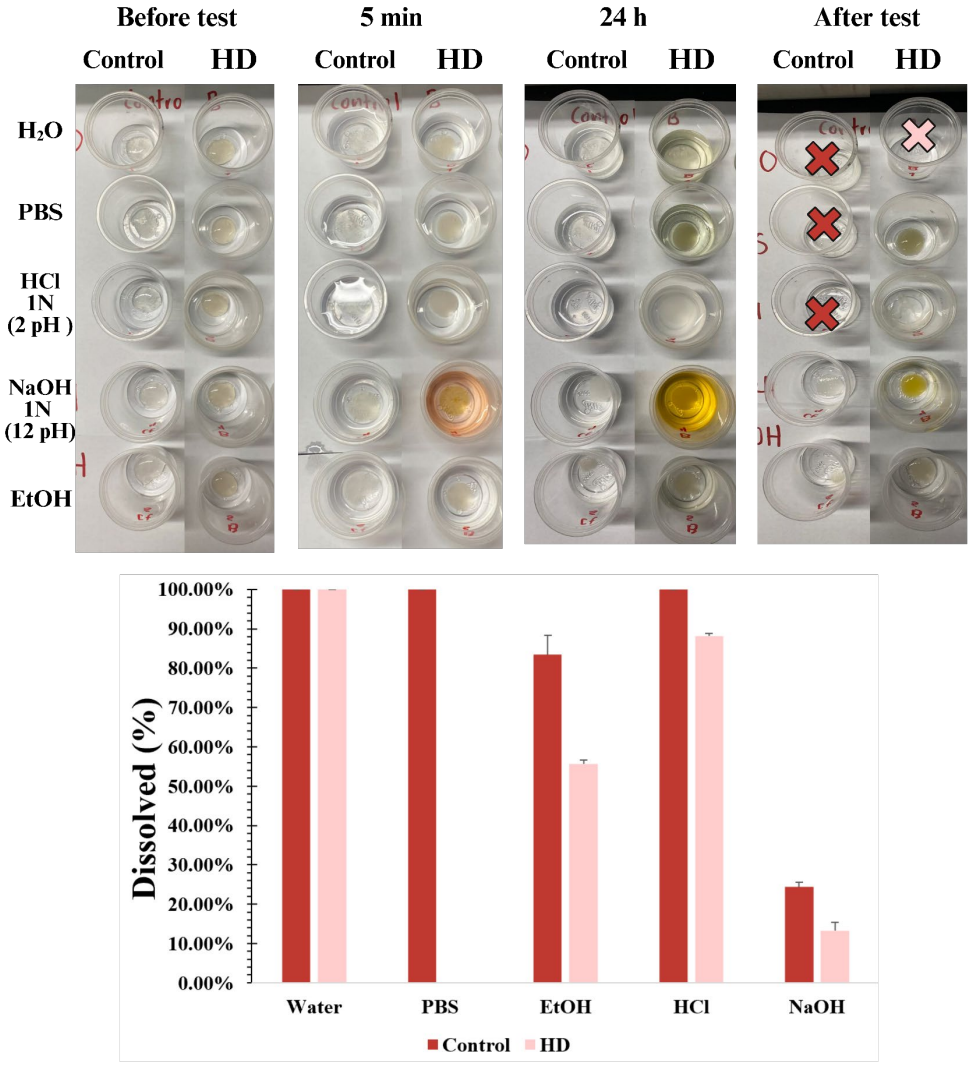

Figure 8. Top) Optical photography of the dissolution of the Control and HD hydrogels in different media over 24 h. A dramatic change is observed within the first 5 min of applying the NaOH solution. The cross indicates that the hydrogel was completely dissolved in the study medium. Down) Dissolution percentage of Control and HD hydrogels in the different media used. Data are presented as mean ± SD, n=3.

 doi:10.20944/preprints202602.1380.v1

In alkaline medium, dissolution was markedly reduced (Control: 24.33%; HD: 11.32%). The HD hydrogel exhibited a reddish-orange coloration, attributed to TA oxidation under basic conditions. The formation of quinone structure may promote additional covalent interactions with amino groups in Gel and Col, reinforcing the network and limiting degradation [53]. This behavior highlights the dynamic adaptability of the system under pH variations.

Thus, this accelerated oxidation suggested that tannic acid was activated in the presence of hydroxyl groups, generating products such as quinines and mostly quinones, which are susceptible to stabilizing with the amino groups in the polymeric network. At this point, there was a new cross-linking with sodium ions and the results of AT oxidation, which compacted the hydrogel. For this reason, the hydrogels did not undergo significant dissolution (Control − 24.33%, HD − 11.32%).

Moreover, exposure to 70% v/v ethanol resulted in significant dissolution (Control: 88%; HD: 55.63%). The reduced stability in EtOH is consistent with disruption of hydrogen bonding interactions and decreased hydration of the polymer network. Nevertheless, the HD hydrogel retained greater structural integrity compared to the Control, further supporting the stabilizing effect of its multi-network architecture.

Collectively, these results demonstrate that HD exhibits enhanced chemical stability across varied environments, particularly under physiological and alkaline conditions, confirming the synergistic contribution of dynamic covalent bonds, ionic interactions, and hydrogen bonding within the hydrogel network. In addition to these physicochemical parameters, the porosity, cross-linking behavior, types of bonds, and mechanical stabilization play important roles in developing innovative bone-promoting healing materials [72].

3.3.3. Adhesion and Surface Interaction Behavior

The adhesion performance of the hydrogels was evaluated on polar and non-polar substrates, including paper, cardboard, alum, silicone, fabric, rubber, plastic and human skin (Figure 9, Video S3). Both formulations adhered to most tested surfaces; however, differences were observed in detachment behavior. On porous substrates such as paper and cardboard, the Control hydrogel left visible residues upon removal, suggesting weaker cohesive integrity. On the other hand, HD hydrogel demonstrated cleaner detachment while maintaining structural continuity. Meanwhile, on fabric, both hydrogels exhibited strong adhesion due to fiber entanglement and increased contact area, preventing complete removal.

When tested on rubber, aluminum, and skin, both hydrogels adhered effectively and could be removed without damaging the surface. Notably, the HD hydrogel exhibited superior handling properties, combining strong adhesion with controlled detachment upon rapid peeling.

However, skin compatibility was evaluated after 10 h of contact (Figure 10a). No irritation, inflammation, or discomfort was observed. Upon removal, the skin appeared hydrated and smooth, likely due to moisture transfer from the hydrogel matrix. After drying, both hydrogels formed a flexible protective layer capable of stretching with skin movements without detaching (Figure 10b).

On the other hand, Figure S2 shows the mechanism of addition with charged amide-type functional groups from the skin surface between the free groups of the hydrogel. The results proposed that catechol-provided functional groups by the TA generated hydrogen bonds between the hydrogel [73]. It is well known that polyphenolic groups exhibit high adhesiveness to the human tissue surface [34], proposing that dynamic covalent bonds with amino and thiol groups take place on the skin surface through Michael addition and Schiff base reactions [74,75]. On the other hand, the adhesion and peel-off ability on human skin was repeatedly evaluated (>12 cycles). This evaluation of the superior and repeatable adhesiveness of HD hydrogel even after the tested cycles.

Contact angle measurements (Figure 10c) showed values of 16.36° (Control hydrogel) and 18.10° (HD hydrogel), confirming the hydrophilic nature of both systems (θ <90°). High wettability supports adhesion, exude absorption, and interfacial hydrogen bonding with tissue surfaces. The enhanced adhesion of HD is attributed to catechol functionalities from TA, with promoted hydrogen bonding and dynamic covalent interactions with amino and thiol groups present in skin proteins [76,77].

 doi:10.20944/preprints202602.1380.v1

In applications for the treatment of open fractures that require activating the process of angiogenesis and subsequent osteoblastic proliferation, it is attractive that the hydrogel takes both shape and the relief of the bone defect to be repaired, integrating with the surrounding connective and vascular tissues. In this way, the process of surgical removal can be avoided due to its ability to detach easily before and after generating a protective layer with a permeable capacity [8,78].

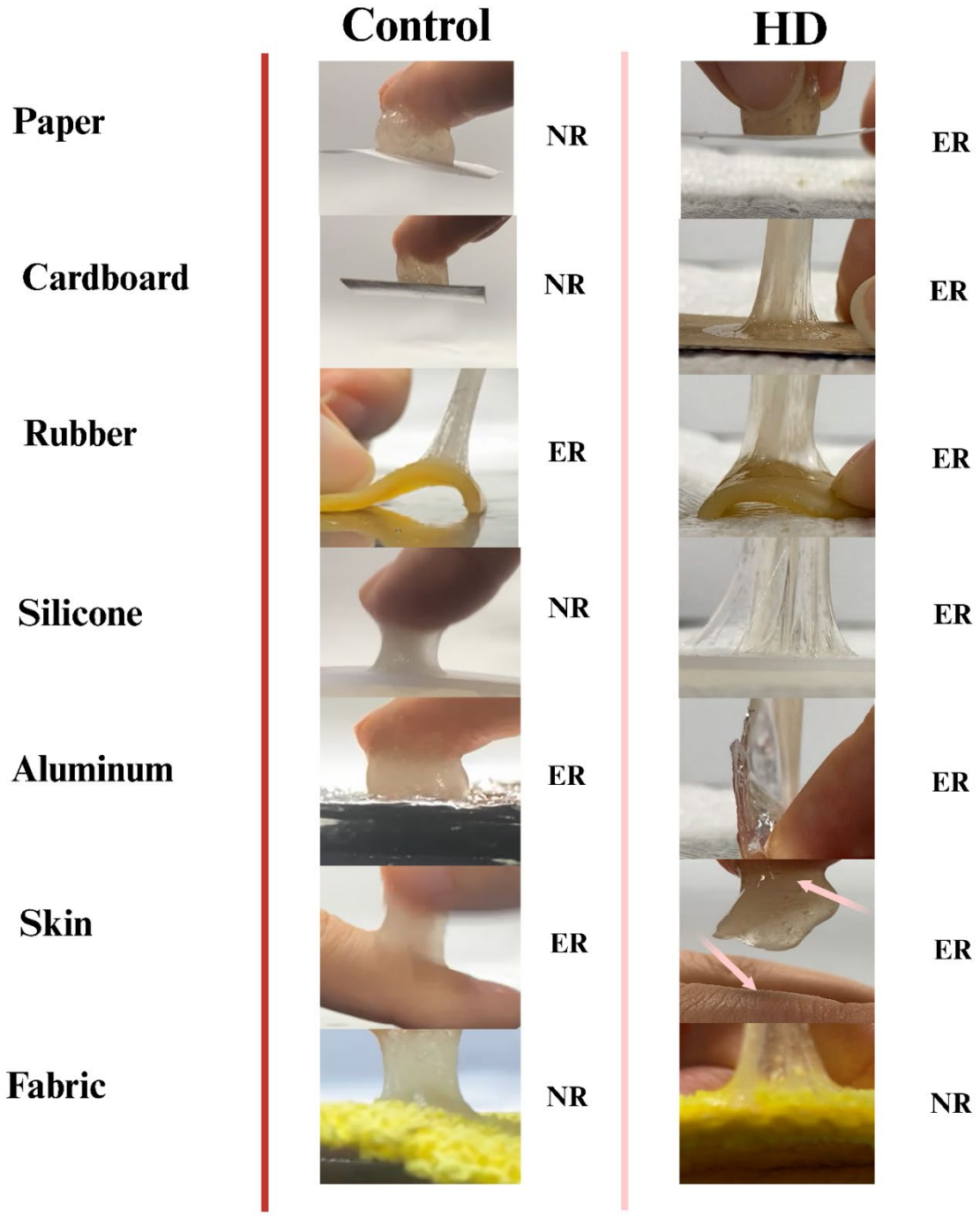

Figure 9. Adhesion test on different surfaces, demonstrating the hydrogel's strong ability to maintain its bonds even after attempts to remove it, causing it to stretch until it peels off. The pink arrows indicate adhesion to human skin, as well as its quick and clean, traceless detachment. NR = Does not come off, and ER = Easy to remove.

 doi:10.20944/preprints202602.1380.v1

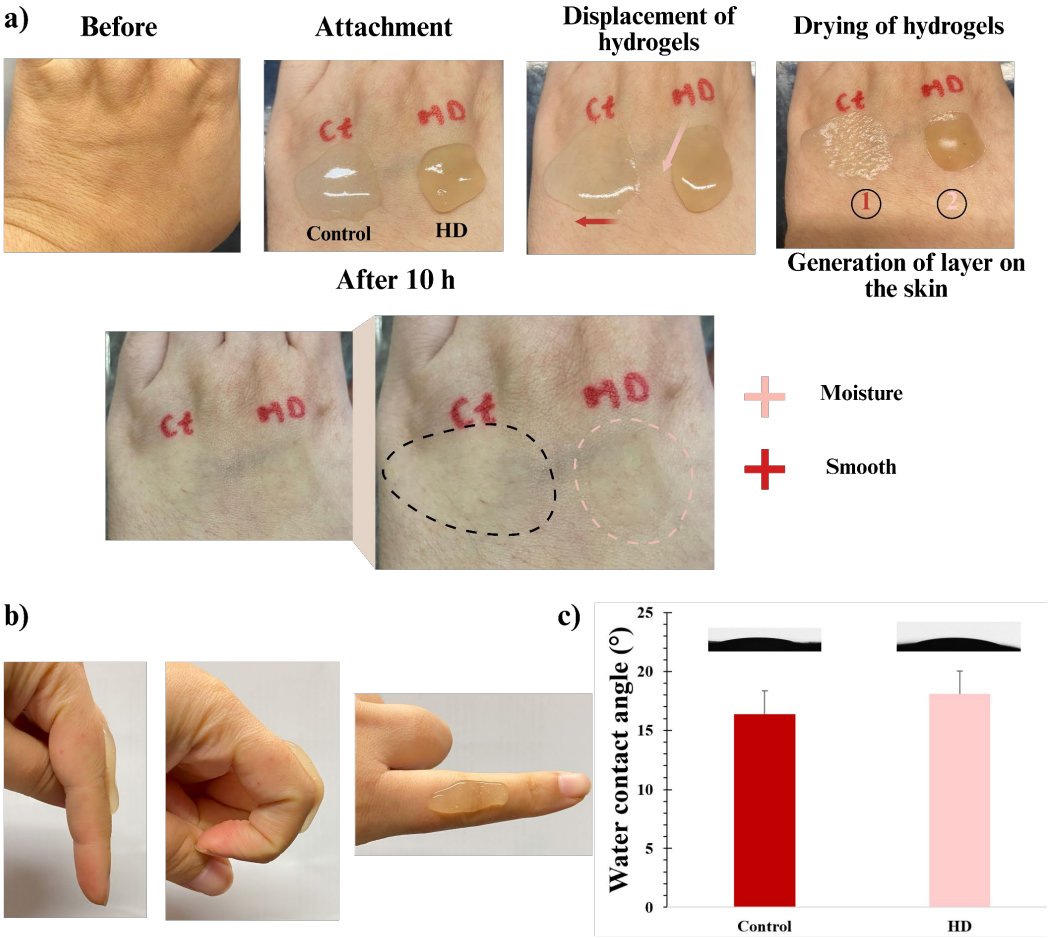

Figure 10. a) Application of hydrogels to the skin for 10 h. Process before and after removal from the skin. The arrows indicate the movement of the hydrogel due to the effect of gravity and the same everyday movements when using it on the extremity. Red and pink arrows correspond to the control and HD hydrogels, respectively. The marked numbering shows the order in which the hydrogels dried until a protective layer was generated. Dotted circles correspond to the position in which the hydrogels were placed, highlighting a smoother and more moisturized appearance. b) Flexion of the HD hydrogel for several cycles, without losing its adhesiveness. c) Wettability of the hydrogels. Data are presented as mean ± SD, n=3.

3.3.4. Water Adhesion

The influence of water on adhesion was evaluated through immersion and fingertip contact experiments (Video S4). The HD hydrogel maintained previously formed interfacial bonds even after brief water exposure, whereas the Control hydrogel detached more readily.

Water exposure temporarily reduced adhesion capacity due to the formation of an interfacial hydration layer, which limits effective polymer-substrate interactions. However, once dried, both hydrogels recovered their adhesive properties, demonstrating reversible interfacial bonding.

The improved wet-surface stability of HD hydrogel is attributed to the synergistic contribution of hydrogen bonding, catechol-mediated interactions, and dynamic borate crosslinking, which collectively preserve cohesive integrity under hydrated conditions [79–81].

3.3.5. Temperature Responsiveness

Thermal stability was evaluated under controlled heating conditions (Figure 11a). The Control hydrogel lost structural firmness at approximately 62 °C, whereas HD maintained structural integrity up to 69 °C. Both hydrogels remained stable at physiological temperature (37 °C). The improved thermal resistance of HD is associated with its multi-network configuration, combining hydrogen

 doi:10.20944/preprints202602.1380.v1

bonding, ionic interactions (for MnP particles), and borate-diol crosslinks. On the other hand, Gel and Col based systems are typically thermoreversible; however, the incorporation of additional crosslinking mechanism enhances thermal tolerance [8,82].

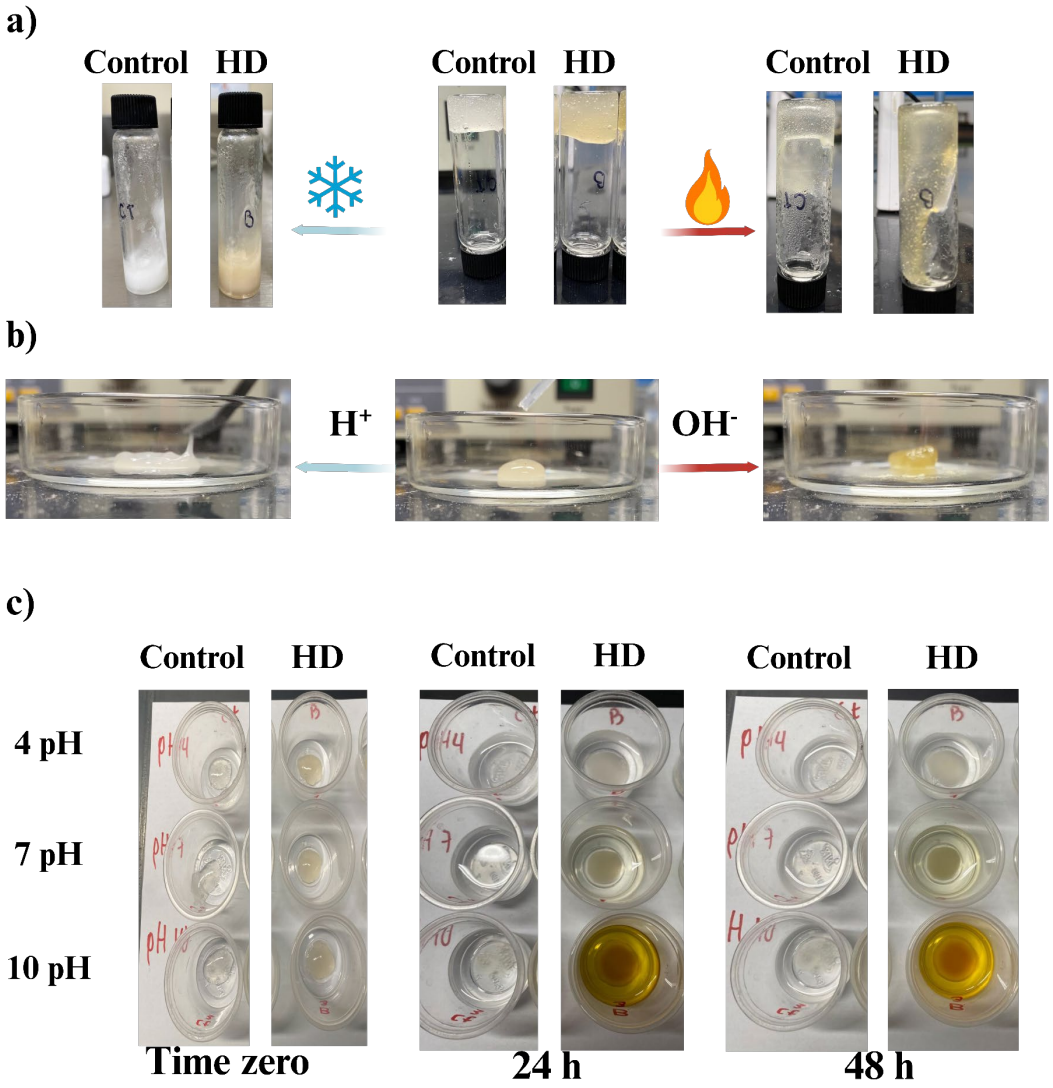

Figure 11. Digital photography of the state of the hydrogels after being subjected to a) temperature changes, b) direct pH changes, c) constant changes for 24 and 48 h in buffers of 4, 7 and 10 pH.

Likewise, HD could withstand and remain in storage at −16 °C without freezing after decreasing the temperature, while the Control could withstand up to −18 °C. The presence of Gli likely contributes to freezing-point depression and improved low-temperature stability [83,84].

3.3.6. pH Responsiveness

We tested the hydrogel under different pH conditions to evaluate the gelation process as a function of the acid/alkaline behavior. Figure 11b showed that the materials lose the hydrogel properties upon ionization in an acidic medium. This effect can be explained due to the B–O$^-$ groups protonating to −B−H, forming a borax-diol complex, which was inefficient and caused the gel's transformation [49,63]. On the other hand, it is necessary to consider the undesirable contribution of boric acid, which was able to adhere to the PVA and GG chains creating inactive elastic sites, hogging spaces in the network, causing a greater dissolution in Control than in HD [85,86]. Similarly, in the hydrogels under pH conditions above 7 − 8, their −B−OH groups were deprotonated to −B−O$^-$ groups that reacted rapidly with guar gum and PVA through diol complexation (as previously described),

 doi:10.20944/preprints202602.1380.v1

leading to efficient gelation. Moreover, the excess of OH^- ions in solution and the OH groups on the PVA main chain were sequentially altered, inducing partial deprotonation and changing the OH group to O−Na (alcoholate) [87,88]. Thus, Bx and GG have a higher affinity to release Na^+ once the O−B−O bond is formed [88], showing fewer functional groups remaining free to interact with any substrate, as observed in Video S5 after replicating the HD hydrogel with the addition of NaOH in its formulation.

The hydrogels were in contact for 48 h with three different Buffers (pH 4.01, 7.0, and 10.01) (Figure 11c). Nonetheless, the tests suggested that the hydrogels did not dissolve completely compared to the results obtained when exposed to highly acidic and alkaline media (Figure 8). This information suggests that pH plays a mandatory role in the structural modulation of the hydrogel, allowing it to retain a defined structure and possible controlling the ions availability that can lead to the formation of a stable cellular microenvironment promoting osteoblastic regeneration.

In this test, a greater expansion of the hydrogels was observed at pH 10.0 through the repulsion between the negatively charged borate ions with the anionic component of the alkaline buffer. Moreover, the enlarged intra-network spaces allow a higher entry of buffer solution into the hydrogel than in the neutral and acidic medium [46]. Also, a copper coloration was observed in both the HD hydrogel and the solvent, derived from the deprotonation of phenolic groups that conducted the formation of less oxidative products compared to pH 12, as well as less soluble tannate salts. The hydrogels close to 7.0 shrink, protecting the internal polymeric network due to the balance of dissolved salts in the buffer solution, allowing a reduction in the osmotic pressure once equilibrium is reached [69]. In acidic media, a higher dissolution was observed in the Control compared to HD, suggesting that the HD hydrogel was the most stable material under the experimental solutions. Thus, between 24 and 48 h, no relevant changes were observed between the samples. Therefore, the structural modulation observed under acidic conditions may favor the availability of Mn-containing species within the local environment and promoting wound healing [89].

3.4. Cell Testing

3.4.1. Cytocompatibility Assessment

The cytocompatibility of the hydrogels was evaluated using MC3T3-E1 pre-osteoblast cells in direct contact conditions (Figure 12a). After 24 h, the negative control medium exhibited the highest metabolic activity, as expected in the absence of material-induced modulation. Both hydrogel formulations maintained substantial cell viability, indicating absence of acute cytotoxic effects. In addition, it is essential to consider that the first 24 h are crucial to allow the first steps of cell adhesion, which affects the microenvironment change due to the presence of the materials, as identified by metabolic activity [90].

Although the HD hydrogel showed slightly lower metabolic activity compared to the Control hydrogel at 24 h, cell viability remained within acceptable biological ranges, suggesting that the incorporation of MnP micro/nanoparticles does not induce detrimental cytotoxicity [40]. Previous studies have reported that MnP nanoparticles exhibit concentration-dependent effects on osteoblast viability, with moderate Mn^{+2} levels promoting differentiation rather than rapid proliferation [39]. This behavior may explain the modest reduction in early metabolic activity observed for HD.

Cell morphology analysis (Figure 12b) revealed well-defined nuclei and extensive cytoplasmic spreading in both treatments. Notably, cells exposed to HD hydrogel displayed pronounced filopodia extension and enhanced cell-cell interactions, indicative of active adhesion and early differentiation processes. In contrast, the Control hydrogel group showed flattened morphology with fewer filopodial structures and occasional vacuole formation.

 doi:10.20944/preprints202602.1380.v1

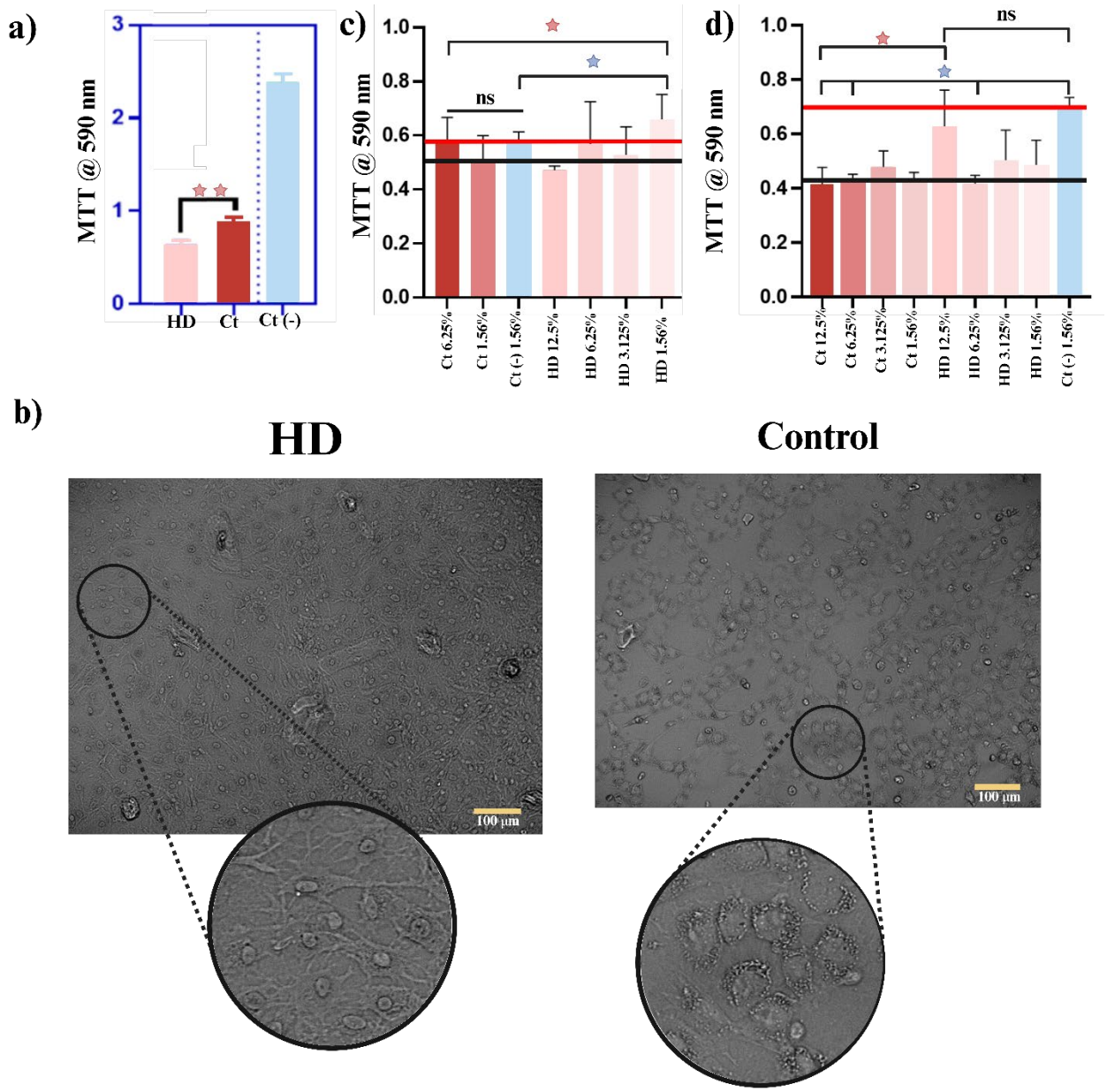

Figure 12. a) Cytotoxicity assays on MC3T3-E1 cells directly in the experimental hydrogels. (★) Show a significant difference compared between HD and Control (Ct) hydrogels, $p < 0.05$. b) Optical microscope images of the cell monolayer formed after removal from the hydrogels (★) compared between Ct and HD with Ct (−). The scale is 100 µm. c) Cell viability assay on MC3T3-E1 at different concentrations of the control and HD hydrogels before the Scratch assay. The black and red lines delimit the maximum values obtained in the Ct and control (−) at a concentration of 1.56% for comparative purposes, respectively. d) Cytotoxicity assays on MC3T3-E1 cells after the Scratch test on the control and HD hydrogels at different concentrations. No significant difference (ns). Data are presented as mean ± SD, n=4. Statistical analysis was carried out using a one-way ANOVA followed by a post-hoc Tukey test (*$p < 0.05$, **$p < 0.01$).

3.4.2. Scratch Assay and Cell Migration

In vitro viability and healing assays were performed before and after performing scratch tests (Figure 12c and d), following the single cell migration assay using the Control and HD hydrogel at different concentrations [29,91]. The 24 h results revealed that the HD hydrogel at 1.56% concentration obtained higher cell migration than the controls (Control (−) and Control hydrogel) at the same polymeric concentration, with significant differences. Likewise, after the scratch test, all concentrations of the HD hydrogel showed healing capacity, with most pronounced effect observed

 doi:10.20944/preprints202602.1380.v1

at 12.5%. At this concentration, no statistical significance was found compared to the Control (−), whereas a significant difference was observed relative to the Control hydrogel. Moreover, the cellular micrographs revealed a displacement and migration of the morphology of the cell.

According to the results, at a concentration of 6.25% in all cases, there was wound closure of 61.99% for Control (−) and 56.77% for the Control hydrogel, while HD showed the lowest value at 45.50%. These findings demonstrate that HD hydrogel can promote cell proliferation and migration. However, the incorporation of manganese phosphate ions slowed down the closure of the scratch; nevertheless, both manganese and phosphate ions are known to support wound healing by regulating osteoblast differentiation at early stages, which prompts the cells to shift their functional activity [92,93]. This phenomenon showed that the contribution of Gel and Col favored MC3T3-E1 cells since they contain bioactive peptides that benefited cell proliferation. By conjugating all the elements in the hydrogel, the osteoblast's viability, migration, wound healing, and proliferation properties were promoted, thus far proposing an improved microenvironment for the cells by stimulating bone-forming functionality [8,94–96].

4. Conclusions

Chitosan-stabilized MnP micro/nanoparticles were successfully synthesized through a CS/AA-assisted route, forming spherical to quasi-spherical domains with nanoscale fractions confirmed by DLS analysis and SEM observations. The multimodal particle size distribution, combined with stable colloidal behavior, supports effective nucleation and stabilization of MnP with the polymeric environment. FITR and EDS analyses confirmed phosphate incorporation and interfacial interactions between Mn^{+2} species and CS functional groups, validating the formation of a hybrid organic-inorganic nanostructured phase suitable for integration into hydrogel matrices.

A multifunctional guar gum/PVA-based hydrogel incorporating these MnP micro/nanoparticles was subsequently developed, exhibiting a highly porous and hydrated structure, pronounced non-Newtonian shear-thinning behavior, and efficient self-healing capacity confirmed by both macroscopic reconnection and rheological step-strain recovery. The integration of reversible borate-diols bonds, hydrogen bonding interactions, and MnP-mediated ionic coordination generated a multi-network architecture capable of dissipating mechanical stress while maintaining structural integrity.

Compared to the Control formulation, the HD hydrogel demonstrated improved swelling tolerance, enhanced stability under physiological and alkaline environments, and superior structural resilience across varied chemical stimuli. The material also exhibited effective bonding with controlled detachment and high wettability.

Biological evaluation confirmed cytocompatibility with MC3T3-E1 pre-osteoblast cells. While slight modulation of early metabolic activity was observed, HD hydrogel supported cellular adhesion, morphological organization, and concentration-dependent migration. The incorporation of MnP micro/nanoparticles influenced early cellular responses without inducing cytotoxicity, suggesting potential osteogenic functionality.

Overall, the synergistic integration of nanostructured MnP particles within a dynamically crosslinked polymeric matrix resulted in a mechanically adaptive, stimuli- responsive, and biologically compatible hydrogel system. These findings position the developed nanostructured hydrogel as a promising platform for bone tissue engineering applications, particularly in environments requiring structural adaptability, adhesion, and pH responsiveness. Further studies focusing on long-term osteogenic differentiation, ion release kinetics, and in vivo performance are warranted to validate its regenerative potential

Supplementary Materials: The following supporting information can be downloaded at the website of this paper posted on Preprints.org, Figure S1: Strain sweep graphs for Control (left) and HD (right) hydrogels. Figure S2: Schematic representation of the interactions between the formulated HD hydrogel and the skin. Created with BioRender.com. Video S1: Hydrogel recovery and self-healing test. Video S3: Rheological behavior of hydrogels

 doi:10.20944/preprints202602.1380.v1

under low and high stresses. Both hydrogels had the same behavior. Video S4: Adhesion tests on different surfaces. Video S5: Hydrogel HD original formula and with extra NaOH - Behavior and cohesion.

Author Contributions: Conceptualization, B.V.-S. and K.G.-C.; methodology, B.V.-S. and K.G.-C.; investigation, B.V.-S., K.G.-C. and J.S.-C.; software, J.S.S.-C., M.C.-Á., N.C. and J.C.-G.; resources, B.V.-S. and K.G.-C.; writing—original draft preparation, B.V.-S., K.G.-C. and E.B.-P.; writing—review and editing, E.B.-P., M.C.-Á. and J.S.-C.; supervision, B.V.-S. and E.B.-P.; formal analysis, K.G.-C., J.S.S.-C., J.C.-G.; visualization, K.G.-C.; validation, B.V.-S., K.G.-C. and J.S.-C.; project administration, K.G.-C. All authors have read and agreed to the published version of the manuscript. All authors have read and agreed to the published version of the manuscript.

Data Availability Statement: The data that support the findings of this study are available from the corresponding author upon reasonable request.

Acknowledgments: We thank to Instituto de Ingeniería of Universidad Autónoma de Baja California, and CONACHYT. Special thanks to Natalia Alvarez.

Conflicts of Interest: The authors declare no conflicts of interest.

References

1. Puppi, D.; Chiellini, F.; Piras, A.M.; Chiellini, E. Polymeric materials for bone and cartilage repair. *Prog. Polym. Sci.* **2010**, 35, 403–440. https://doi.org/10.1016/j.progpolymsci.2010.01.006
2. Bai, X.; Gao, M.; Syed, S.; Zhuang, J.; Xu, X.; Zhang, X.-Q. Bioactive hydrogels for bone regeneration. *Bioact. Mater.* **2018**, 3, 401–417. https://doi.org/10.1016/j.bioactmat.2018.05.006
3. Sop, J.L.; Sop, A. Open Fracture Management. StatPearls Publishing: Treasure Island, FL, USA, 2023. Available online: http://europepmc.org/books/NBK448083 (accessed on 17 September 2025).
4. Dheenadhayalan, J.; Nagashree, V.; Devendra, A.; Velmurugesan, P.S.; Rajasekaran, S. Management of open fractures: A narrative review. *J. Clin. Orthop. Trauma* **2023**, 44, 102246. https://doi.org/10.1016/j.jcot.2023.102246
5. Fibbe, W.E.; Dazzi, F.; LeBlanc, K. MSCs: science and trials. *Nat. Med.* **2013**, 19, 812–813. https://doi.org/10.1038/nm.3222
6. García-Gareta, E.; Coathup, M.J.; Blunn, G.W. Osteoinduction of bone grafting materials for bone repair and regeneration. *Bone* **2015**, 81, 112–121. https://doi.org/10.1016/j.bone.2015.07.007
7. Ansari, M. Bone tissue regeneration: biology, strategies and interface studies. *Prog. Biomater.* **2019**, 8, 223–237. https://doi.org/10.1007/s40204-019-00125-z
8. Guillén-Carvajal, K.; Valdez-Salas, B.; Beltrán-Partida, E.; Salomón-Carlos, J.; Cheng, N. Chitosan, gelatin, and collagen hydrogels for bone regeneration. *Polymers* **2023**, 15, 2762. https://doi.org/10.3390/polym15132762
9. Muir, V.G.; Burdick, J.A. Chemically modified biopolymers for the formation of biomedical hydrogels. *Chem. Rev.* **2021**, 121, 10908–10949. https://doi.org/10.1021/acs.chemrev.0c00923
10. Zhang, Y.; Yu, T.; Peng, L.; Sun, Q.; Wei, Y.; Han, B. Advancements in hydrogel-based drug sustained release systems for bone tissue engineering. *Front. Pharmacol.* **2020**, 11, 00622. https://doi.org/10.3389/fphar.2020.00622
11. Zhang, Y.; Li, Z.; Guan, J.; Mao, Y.; Zhou, P. Hydrogel: A potential therapeutic material for bone tissue engineering. *AIP Adv.* **2021**, 11, 015006. https://doi.org/10.1063/5.0035504
12. Khan, S.; Maryam, L.; Gulzar, A.; Mansoor, M.A.; Iqbal, M. Smart and active hydrogels in biotechnology—synthetic techniques and applications. *J. Mater. Sci.* **2024**, 59, 16449–16471. https://doi.org/10.1007/s10853-024-10187-5
13. Liu, J.; Du, C.; Huang, W.; Lei, Y. Injectable smart stimuli-responsive hydrogels: pioneering advancements in biomedical applications. *Biomater. Sci.* **2024**, 12, 8–56. https://doi.org/10.1039/D3BM01352A
14. Mahinroosta, M.; Jomeh Farsangi, Z.; Allahverdi, A.; Shakoori, Z. Hydrogels as intelligent materials: synthesis, properties and applications. *Mater. Today Chem.* **2018**, 8, 42–55. https://doi.org/10.1016/j.mtchem.2018.02.004

15. Bode, F.; da Silva, M.A.; Drake, A.F.; Ross-Murphy, S.B.; Dreiss, C.A. Enzymatically cross-linked tilapia gelatin hydrogels. *Biomacromolecules* **2011**, 12, 3741–3752. https://doi.org/10.1021/bm2009894
16. Saravanan, S.; Vimalraj, S.; Anuradha, D. Chitosan based thermoresponsive hydrogel containing graphene oxide for bone tissue repair. *Biomed. Pharmacother.* **2018**, 107, 908–917. https://doi.org/10.1016/j.biopha.2018.08.072
17. Iqbal, D.N.; et al. Novel chitosan/guar gum/PVA hydrogel: Preparation, characterization and antimicrobial activity evaluation. *Int. J. Biol. Macromol.* **2020**, 164, 499–509. https://doi.org/10.1016/j.ijbiomac.2020.07.139
18. Guo, N.; Zhang, L.; Wang, J.; Wang, S.; Zou, Y.; Wang, X. Gelatin/chitosan bio-composited hydrogel system to accelerate bone fracture healing. *Process Biochem.* **2020**, 90, 177–183. https://doi.org/10.1016/j.procbio.2019.11.016
19. Sethi, S.; Medha; Kaith, B.S. Chitosan-gelatin nanocomposites: Synthesis and biomedical applications. *React. Funct. Polym.* **2022**, 179, 105362. https://doi.org/10.1016/j.reactfunctpolym.2022.105362
20. Sarrigiannidis, S.O.; Rey, J.M.; Dobre, O.; González-García, C.; Dalby, M.J.; Salmeron-Sanchez, M. Collagen hydrogel modifications to improve mechanical and growth factor loading capabilities. *Mater. Today Bio* **2021**, 10, 100098. https://doi.org/10.1016/j.mtbio.2021.100098
21. Yu, J.; Hao, R.; Sheng, F.; Xu, L.; Li, G.; Hou, Y. Hollow manganese phosphate nanoparticles as smart multifunctional probes for cancer cell targeted magnetic resonance imaging and drug delivery. Nano Res. 2012, 5, 679–694. https://doi.org/10.1007/s12274-012-0252-z
22. Wang, M.-Q.; Ye, C.; Bao, S.-J.; Xu, M.-W. Controlled synthesis of $Mn_3(PO_4)_2$ hollow spheres as biomimetic enzymes for selective detection of superoxide anions released by living cells. *Microchim. Acta* **2017**, 184, 1177–1184. https://doi.org/10.1007/s00604-017-2112-8
23. Nawaz, Q.; et al. Synthesis and characterization of manganese containing mesoporous bioactive glass nanoparticles for biomedical applications. *J. Mater. Sci. Mater. Med*. **2018**, 29, 64. https://doi.org/10.1007/s10856-018-6070-4
24. Barrioni, B.R.; Norris, E.; Li, S.; Naruphontjirakul, P.; Jones, J.R.; Pereira, M.M. Osteogenic potential of sol–gel bioactive glasses containing manganese. *J. Mater. Sci. Mater. Med.* **2019**, 30, 86. https://doi.org/10.1007/s10856-019-6288-9
25. Westhauser, F.; et al. Effect of manganese, zinc, and copper on the biological and osteogenic properties of mesoporous bioactive glass nanoparticles. *J. Biomed. Mater. Res. A* **2021**, 109, 1457–1467. https://doi.org/10.1002/jbm.a.37136
26. Valdez-Salas, B.; et al. Promotion of surgical masks antimicrobial activity by disinfection and impregnation with disinfectant silver nanoparticles. *Int. J. Nanomedicine* **2021**, 16, 2689–2702. https://doi.org/10.2147/IJN.S301212
27. Valdez-Salas, B.; et al. Structure–activity relationship of diameter controlled Ag@Cu nanoparticles in broad-spectrum antibacterial mechanism. *Mater. Sci. Eng. C* **2021**, 119, 111501. https://doi.org/10.1016/j.msec.2020.111501
28. Khamrai, M.; Banerjee, S.L.; Paul, S.; Samanta, S.; Kundu, P.P. Curcumin entrapped gelatin/ionically modified bacterial cellulose based self-healable hydrogel film. *Int. J. Biol. Macromol*. **2019**, 122, 940–953. https://doi.org/10.1016/j.ijbiomac.2018.10.196
29. ElSayed, N.S.; Helmy, N.M.; Kamel, S. Dual-adhesive and self-healing alginate-based hydrogel for wound healing. *Chem. Pap.* **2024**, 78, 1021–1031. https://doi.org/10.1007/s11696-023-03140-4
30. Sreedevi Madhavikutty, A.; Singh Chandel, A.K.; Tsai, C.-C.; Inagaki, N.F.; Ohta, S.; Ito, T. pH responsive cationic guar gum-borate self-healing hydrogels for muco-adhesion. *Sci. Technol. Adv. Mater.* **2023**, 24, 2175586. https://doi.org/10.1080/14686996.2023.2175586
31. Homez-Jara, A.; Daza, L.D.; Aguirre, D.M.; Muñoz, J.A.; Solanilla, J.F.; Váquiro, H.A. Characterization of chitosan edible films obtained with various polymer concentrations and drying temperatures. *Int. J. Biol. Macromol.* **2018**, 113, 1233–1240. https://doi.org/10.1016/j.ijbiomac.2018.03.057
32. Zu, Y.; et al. Preparation and characterization of chitosan–polyvinyl alcohol blend hydrogels for the controlled release of nano-insulin. *Int. J. Biol. Macromol.* **2012**, 50, 82–87. https://doi.org/10.1016/j.ijbiomac.2011.10.006

 doi:10.20944/preprints202602.1380.v1

33. Pérez-Díaz, M.; et al. Anti-biofilm activity of chitosan gels formulated with silver nanoparticles and their cytotoxic effect on human fibroblasts. *Mater. Sci. Eng. C* **2016**, 60, 317–323. https://doi.org/10.1016/j.msec.2015.11.036
34. Su, X.; et al. Ctenophore-inspired hydrogels for efficient and repeatable underwater specific adhesion to biotic surfaces. *Mater. Horiz.* **2020**, 7, 2651–2661. https://doi.org/10.1039/D0MH01344G
35. Valdez-Salas, B.; et al. Recovering osteoblast functionality on TiO_2 nanotube surfaces under diabetic conditions. *Int. J. Nanomedicine* **2022**, 17, 5469–5488. https://doi.org/10.2147/IJN.S387386
36. Rivera-Martinez, T.; Valdez-Salas, B.; Salvador-Carlos, J.; Stoytcheva, M.; Zlatev, R.; Beltrán-Partida, E. Improvement of the antibacterial and skin-protective performance of alcohol-based sanitizers using hydroglycolic phytocompounds. *Biotechnol. Biotechnol. Equip.* **2023**, 37, 2253927. https://doi.org/10.1080/13102818.2023.2253927
37. Alimi, B.A.; Pathania, S.; Wilson, J.; Duffy, B.; Frias, J.M.C. Extraction, quantification, characterization, and application in food packaging of chitin and chitosan from mushrooms: A review. *Int. J. Biol. Macromol.* **2023**, 237, 124195. https://doi.org/10.1016/j.ijbiomac.2023.124195
38. Nandiyanto, A.O.R.R.R. How to read and interpret FTIR spectroscope of organic material. *Indones. J. Sci. Technol.* **2019**, 4, 97–118.
39. Wang, Y.; et al. Constructing high effective nano-$Mn_3(PO_4)_2$-chitosan in situ electrochemical detection interface for superoxide anions released from living cell. *Biosens. Bioelectron.* **2019**, 133, 133–140. https://doi.org/10.1016/j.bios.2019.03.029
40. Rau, J.V.; et al. Sic parvis magna: manganese-substituted tricalcium phosphate and its biophysical properties. *ACS Biomater. Sci. Eng.* ***2019***, 5, 6632–6644. https://doi.org/10.1021/acsbiomaterials.9b01528
41. Jadhav, A.J.; et al. Development of smart nanocontainers with a zinc phosphate core and a pH-responsive shell for controlled release of imidazole. *Hybrid Mater.* **2015**, 2, 1. https://doi.org/10.1515/hyma-2015-0001
42. Jadhav, A.J.; Pinjari, D.V.; Pandit, A.B. Surfactant assisted sonochemical synthesis of hollow structured zinc phosphate nanoparticles and their application as nanocarrier. *Chem. Eng. J.* **2016**, 297, 116–120. https://doi.org/10.1016/j.cej.2016.04.001
43. Mathew, S.A.; Arumainathan, S. Crosslinked chitosan–gelatin biocompatible nanocomposite as a neuro drug carrier. *ACS Omega* **2022**, 7, 18732–18744. https://doi.org/10.1021/acsomega.2c01443
44. Park, S.; Choi, J.; Doan, V.H.M.; O, S.H. Biodegradable manganese-doped hydroxyapatite antitumor adjuvant as a promising photo-therapeutic for cancer treatment. *Front. Mol. Biosci.* **2022**, 9, 1085458. https://doi.org/10.3389/fmolb.2022.1085458
45. Croisier, F.; Jérôme, C. Chitosan-based biomaterials for tissue engineering. *Eur. Polym. J.* **2013**, 49, 780–792. https://doi.org/10.1016/j.eurpolymj.2012.12.009
46. Thombare, N.; Jha, U.; Mishra, S.; Siddiqui, M.Z. Borax cross-linked guar gum hydrogels as potential adsorbents for water purification. *Carbohydr. Polym.* **2017**, 168, 274–281. https://doi.org/10.1016/j.carbpol.2017.03.086
47. Sharma, G.; et al. Guar gum and its composites as potential materials for diverse applications: A review. *Carbohydr. Polym.* **2018**, 199, 534–545. https://doi.org/10.1016/j.carbpol.2018.07.053
48. Chen, M.; et al. Hydrogen bonding impact on chitosan plasticization. *Carbohydr. Polym.* **2018**, 200, 115–121. https://doi.org/10.1016/j.carbpol.2018.07.062
49. Talodthaisong, C.; et al. Composite guar gum-silver nanoparticle hydrogels as self-healing, injectable, and antibacterial biomaterials. *Mater. Today Commun.* **2020**, 24, 100992. https://doi.org/10.1016/j.mtcomm.2020.100992
50. Pan, X.; et al. Ultraflexible self-healing guar gum-glycerol hydrogel with injectable, antifreeze, and strain-sensitive properties. *ACS Biomater. Sci. Eng.* **2018**, 4, 3397–3404. https://doi.org/10.1021/acsbiomaterials.8b00657
51. Yang, S.; Zhang, Y.; Wang, T.; Sun, W.; Tong, Z. Ultrafast and programmable shape memory hydrogel of gelatin soaked in tannic acid solution. *ACS Appl. Mater. Interfaces* **2020**, 12, 46701–46709. https://doi.org/10.1021/acsami.0c13531

 doi:10.20944/preprints202602.1380.v1

52. Nath, J.; Saikia, P.P.; Handique, J.; Gupta, K.; Dolui, S.K. Multifunctional mussel-inspired gelatin and tannic acid-based hydrogel with pH-controllable release of vitamin B12. *J. Appl. Polym. Sci*. **2020**, 137, 49193. https://doi.org/10.1002/app.49193
53. Maier, G.P.; Bernt, C.M.; Butler, A. Catechol oxidation: considerations in the design of wet adhesive materials. *Biomater. Sci.* **2018**, 6, 332–339. https://doi.org/10.1039/C7BM00884H
54. Wang, C.; et al. Facile fabrication and characterization of high-performance borax-PVA hydrogel. *J. Solgel Sci. Technol.* **2022**, 101, 103–113. https://doi.org/10.1007/s10971-021-05584-0
55. Rahmani, S.; Olad, A.; Rahmani, Z. Preparation of self-healable nanocomposite hydrogel based on gum arabic/gelatin and graphene oxide: Study of drug delivery behavior. *Polym. Bull.* **2023**, 80, 4117–4138. https://doi.org/10.1007/s00289-022-04247-6
56. Zuidema, J.M.; Rivet, C.J.; Gilbert, R.J.; Morrison, F.A. A protocol for rheological characterization of hydrogels for tissue engineering strategies. *J. Biomed. Mater. Res. B Appl. Biomater.* **2014**, 102, 1063–1073. https://doi.org/10.1002/jbm.b.33088
57. Guillén-Carvajal, K.M.; et al. Synergistic and intelligent hydrogel for conducting osteoblast proliferation. *Gels* **2025**, 11, 910. https://doi.org/10.3390/gels11110910
58. Stojkov, G.; Niyazov, Z.; Picchioni, F.; Bose, R.K. Relationship between structure and rheology of hydrogels for various applications. *Gels* **2021**, 7, 255. https://doi.org/10.3390/gels7040255
59. Mendoza, L.; Batchelor, W.; Tabor, R.F.; Garnier, G. Gelation mechanism of cellulose nanofibre gels: A colloids and interfacial perspective. *J. Colloid Interface Sci.* **2018**, 509, 39–46. https://doi.org/10.1016/j.jcis.2017.08.101
60. Anton Paar GmbH. Internal structures of samples and shear-thinning behavior. Rheology Wiki. **2025.** Available online: https://wiki.anton-paar.com/sg-en/internal-structures-of-samples-and-shear-thinning-behavior/ (accessed on 17 September 2025).
61. Afzal, S.; Maswal, M.; Dar, A.A. Rheological behavior of pH responsive composite hydrogels of chitosan and alginate: Characterization and its use in encapsulation of citral. *Colloids Surf. B Biointerfaces* **2018**, 169, 99–106. https://doi.org/10.1016/j.colsurfb.2018.05.002
62. Andersen, A.; Krogsgaard, M.; Birkedal, H. Mussel-inspired self-healing double-cross-linked hydrogels by controlled combination of metal coordination and covalent cross-linking. *Biomacromolecules* **2018**, 19, 1402–1409. https://doi.org/10.1021/acs.biomac.7b01249
63. Lu, B.; et al. One-pot assembly of microfibrillated cellulose reinforced PVA–borax hydrogels with self-healing and pH-responsive properties. *ACS Sustain. Chem. Eng.* **2017**, 5, 948–956. https://doi.org/10.1021/acssuschemeng.6b02279
64. Yanagisawa, Y.; Nan, Y.; Okuro, K.; Aida, T. Mechanically robust, readily repairable polymers via tailored noncovalent cross-linking. *Science* **2018**, 359, 72–76. https://doi.org/10.1126/science.aam7588
65. Quan, L.; Xin, Y.; Wu, X.; Ao, Q. Mechanism of self-healing hydrogels and application in tissue engineering. *Polymers* **2022**, 14, 2184. https://doi.org/10.3390/polym14112184
66. Darabi, M.A.; et al. Skin-inspired multifunctional autonomic-intrinsic conductive self-healing hydrogels with pressure sensitivity, stretchability, and 3D printability. *Adv. Mater.* **2017**, 29, 1700533. https://doi.org/10.1002/adma.201700533
67. Naahidi, S.; et al. Biocompatibility of hydrogel-based scaffolds for tissue engineering applications. *Biotechnol. Adv.* **2017**, 35, 530–544. https://doi.org/10.1016/j.biotechadv.2017.05.006
68. Taheri, S.; et al. Injectable, pore-forming, perfusable double-network hydrogels resilient to extreme biomechanical stimulations. *Adv. Sci.* **2022**, 9, 2102627. https://doi.org/10.1002/advs.202102627
69. Khan, M.U.A.; et al. Development of antibacterial, degradable and pH-responsive chitosan/guar gum/polyvinyl alcohol blended hydrogels for wound dressing. *Molecules* **2021**, 26, 5937. https://doi.org/10.3390/molecules26195937
70. Kokol, V.; Pottathara, Y.B.; Mihelčič, M.; Perše, L.S. Rheological properties of gelatine hydrogels affected by flow- and horizontally-induced cooling rates during 3D cryo-printing. *Colloids Surf. A Physicochem. Eng. Asp.* **2021**, 616, 126356. https://doi.org/10.1016/j.colsurfa.2021.126356

 doi:10.20944/preprints202602.1380.v1

71. Rizwan, M.; et al. pH sensitive hydrogels in drug delivery: Brief history, properties, swelling, and release mechanism, material selection and applications. *Polymers* **2017**, 9, 137. https://doi.org/10.3390/polym9040137
72. Kankala, R.K.; Wang, S.-B.; Chen, A.-Z.; Zhang, Y.S. Self-assembled nanogels: From particles to scaffolds and membranes. In Handbook of Nanomaterials for Cancer Theranostics; *Elsevier: Amsterdam, The Netherlands*, **2018**; pp. 33–62. https://doi.org/10.1016/B978-0-12-813339-2.00002-5
73. Han, L.; Wang, M.; Prieto-López, L.O.; Deng, X.; Cui, J. Self-hydrophobization in a dynamic hydrogel for creating nonspecific repeatable underwater adhesion. *Adv. Funct. Mater*. **2020**, 30, 1907064. https://doi.org/10.1002/adfm.201907064
74. Li, B.; Whalen, J.J.; Humayun, M.S.; Thompson, M.E. Reversible bioadhesives using tannic acid primed thermally-responsive polymers. *Adv. Funct. Mater.* **2020**, 30, 1907478. https://doi.org/10.1002/adfm.201907478
75. Fan, X.; Zhou, W.; Chen, Y.; Yan, L.; Fang, Y.; Liu, H. An antifreezing/antiheating hydrogel containing catechol derivative urushiol for strong wet adhesion to various substrates. *ACS Appl. Mater. Interfaces* **2020**, 12, 32031–32040. https://doi.org/10.1021/acsami.0c09917
76. Mao, G.; et al. Preparation and evaluation of a novel alginate-arginine-zinc ion hydrogel film for skin wound healing. *Carbohydr. Polym.* **2023**, 311, 120757. https://doi.org/10.1016/j.carbpol.2023.120757
77. Xu, M.; Miao, Y.; Yu, J.; Zhang, L. Physiologically-regulated adhesion of hydrogels for wound dressing. *Adv. Mater. Interfaces* **2021**, 8, 2101131. https://doi.org/10.1002/admi.202101131
78. Silva, R.; Fabry, B.; Boccaccini, A.R. Fibrous protein-based hydrogels for cell encapsulation. *Biomaterials* **2014**, 35, 6727–6738. https://doi.org/10.1016/j.biomaterials.2014.04.078
79. Chen, K.; et al. An all-in-one tannic acid-containing hydrogel adhesive with high toughness, self-healability and strong underwater adhesion. *ACS Appl. Mater. Interfaces* **2021**, 13, 9748–9761. https://doi.org/10.1021/acsami.1c00637
80. Shin, M.; Park, E.; Lee, H. Plant-inspired pyrogallol-containing functional materials. *Adv. Funct. Mater.* **2019**, 29, 1903022. https://doi.org/10.1002/adfm.201903022
81. Ma, X.; et al. Hydrogels for underwater adhesion: Adhesion mechanism, design strategies and applications. J. Mater. Chem. A **2022**, 10, 11823–11853. https://doi.org/10.1039/D2TA01960D
82. Yang, Z.; et al. Nonlinear behavior of gelatin networks reveals a hierarchical structure. *Biomacromolecules* **2016**, 17, 590–600. https://doi.org/10.1021/acs.biomac.5b01538
83. Chen, F.; et al. Rational fabrication of anti-freezing, non-drying tough organohydrogels by one-pot solvent displacement. *Angew. Chem. Int. Ed.* **2018**, 57, 6568–6571. https://doi.org/10.1002/anie.201803366
84. Zhou, D.; Chen, F.; Handschuh-Wang, S.; Gan, T.; Zhou, X.; Zhou, X. Biomimetic extreme-temperature- and environment-adaptable hydrogels. *ChemPhysChem* **2019**, 20, 2139–2154. https://doi.org/10.1002/cphc.201900545
85. Narita, T.; Mayumi, K.; Ducouret, G.; Hébraud, P. Viscoelastic properties of poly(vinyl alcohol) hydrogels having permanent and transient cross-links studied by microrheology, classical rheometry, and dynamic light scattering. *Macromolecules* **2013**, 46, 4174–4183. https://doi.org/10.1021/ma400600f
86. Mahjoub, H.F.; Zammali, M.; Abbes, C.; Othman, T. Microrheological study of PVA/borax physical gels: Effect of chain length and elastic reinforcement by sodium hydroxide addition. *J. Mol. Liq*. **2019**, 291, 111272. https://doi.org/10.1016/j.molliq.2019.111272
87. Bejenariu, A.; Popa, M.; Dulong, V.; Picton, L.; Le Cerf, D. Trisodium trimetaphosphate crosslinked xanthan networks: Synthesis, swelling, loading and releasing behaviour. *Polym. Bull.* **2009**, 62, 525–538. https://doi.org/10.1007/s00289-008-0033-8
88. Ingtipi, K.; Choudhury, B.J.; Moholkar, V.S. Development of NaOH-borax crosslinked PVA-xanthan gum-lignin hydrogel as green fire retardant coating. *Prog. Org. Coat.* **2023**, 174, 107268. https://doi.org/10.1016/j.porgcoat.2022.107268
89. Berkmann, J.C.; et al. Early pH changes in musculoskeletal tissues upon injury—Aerobic catabolic pathway activity linked to inter-individual differences in local pH. *Int. J. Mol. Sci.* **2020**, 21, 2513. https://doi.org/10.3390/ijms21072513

 doi:10.20944/preprints202602.1380.v1

90. Zhang, Y. Cell toxicity mechanism and biomarker. *Clin. Transl. Med.* **2018**, 7, 21. https://doi.org/10.1186/s40169-018-0212-7
91. Bektas, N.; Şenel, B.; Yenilmez, E.; Özatik, O.; Arslan, R. Evaluation of wound healing effect of chitosan-based gel formulation containing vitexin. *Saudi Pharm. J.* **2020**, 28, 87–94. https://doi.org/10.1016/j.jsps.2019.11.008
92. Du, M.; et al. Tunable layered (Na,Mn)V_8O_{20}·nH_2O cathode material for high-performance aqueous zinc ion batteries. *Adv. Sci.* **2020**, 7, 2000083. https://doi.org/10.1002/advs.202000083
93. Yang, X.; et al. Coating of manganese functional polyetheretherketone implants for osseous interface integration. *Front. Bioeng. Biotechnol.* **2023**, 11, 1182187. https://doi.org/10.3389/fbioe.2023.1182187
94. Parenteau-Bareil, R.; Gauvin, R.; Berthod, F. Collagen-based biomaterials for tissue engineering applications. *Materials* **2010**, 3, 1863–1887. https://doi.org/10.3390/ma3031863
95. Yang, Z.; Chaieb, S.; Hemar, Y. Gelatin-based nanocomposites: A review. *Polym. Rev.* **2021**, 61, 765–813. https://doi.org/10.1080/15583724.2021.1897995
96. Hoang Thi, T.T.; Lee, Y.; Le Thi, P.; Park, K.D. Oxidized alginate supplemented gelatin hydrogels for the in situ formation of wound dressing with high antibacterial activity. *Macromol. Res.* **2019**, 27, 811–820. https://doi.org/10.1007/s13233-019-7115-3